Stability and Growth Kinetics of {112} Twin Embryos in β-Ti Alloys

Ganlin Chen[1], Dian Li[2,3], Yufeng Zheng[2,3], and Liang Qi*[1]

[1]Department of Materials Science and Engineering, University of Michigan, Ann Arbor, 48109, MI, USA

[2]Department of Chemical and Materials Engineering, University of Nevada Reno, Reno, 89557, NV, USA

[3]Department of Materials Science and Engineering, University of North Texas, Denton, 76205, TX, USA

*Corresponding author: qiliang@umich.edu

Abstract

$\{112\}\langle 11\bar{1}\rangle$ deformation twin, shortened as $\{112\}$ twin, is usually the dominant twinning mode in transition metal alloys in a body-centered cubic (BCC) lattice except for many BCC β titanium (Ti) alloys. To understand this twin-mode variation, we investigate stability and early-stage growth kinetics of $\{112\}$ twin embryos with multiple atomic layers in a series of β-Ti alloys by applying density functional theory (DFT) and classical atomistic simulations. Both simulation methods demonstrate that, as average valence electron concentration (VEC measured in a unit of e/a) of Ti alloys decreases, $\beta \rightarrow \omega$ phase transformations at $\{112\}$ twin boundaries, which are confirmed by our transmission electron microscopy characterizations, increase the critical thickness of $\{112\}$ layers as stable twin embryos, possibly raising $\{112\}$ twin nucleation energy barriers. In simulations of twin embryo growths under applied shear stress on $\{112\}$ planes, when VEC (or temperature) values are low ($\sim$4.25 e/a at 300 K), the applied shear stress results in β twin $\rightarrow \alpha$'/α" phase $\rightarrow \beta$ matrix phase transformations through an anti-twinning mechanism inside the existing twin embryos; concurrently, ω phases strongly impede the twin boundary migration; these combined effects result in eliminations of $\{112\}$ twin embryos. However, when VEC increases slightly ($\sim$4.34 e/a at 300 K), ω phases at twin boundaries reduce the required stress for $\{112\}$ twin embryo growth compared with the cases with high VEC values (e.g., $\sim$4.50 e/a at 300 K). These changes of ω effects on $\{112\}$ twin embryo growth kinetics could originate from free energy landscape variations of β matrix $\rightarrow \omega$ phase $\rightarrow \beta$ twin phase transformations.

1 Introduction

β titanium (Ti) alloys in body-centered cubic (BCC) lattice are important for many industrial applications [1–5], such as aerospace, healthcare, and power generations [3, 4, 6, 7]. Depending on thermomechanical processes, phases with different crystal structures can be observed in β-Ti alloys, e.g., β phase in BCC lattice, α' phase in hexagonal close-packed (HCP) structure, α" phase in an orthorhombic lattice, and ω phase in a hexagonal lattice, plotted in Figure 1 (a-b). The diffusionless transformations between β and other phases can induce large plastic strain, which is the underlying mechanism of the shape memory effect and superior plasticity in some β-Ti alloys [8–12]. There are also multiple types of deformation twinning modes in β-Ti alloys that may play different roles in plastic deformation depending on alloy compositions and deformation conditions [8, 9]. For example, $\{112\}\langle 11\bar{1}\rangle$ twin (shortened as $\{112\}$ twin in the following sections), commonly observed as the major deformation twinning mode in conventional BCC transition metals [13], is not the leading twinning mode in many β-Ti alloys [14–18]. Meanwhile, twinning modes with highly-indexed (Miller indices larger than 2) twin-boundary planes (so-called highly-indexed twinning), especially $\{332\}\langle 11\bar{3}\rangle$ twin (shortened as $\{332\}$ twin in the following sections), can be activated and act as the dominate twinning mode in many β-Ti alloys [17, 19–23]. Extensive studies have shown the exceptional performances of highly-indexed twinning in improving mechanical properties of β-Ti alloys [17, 19, 24–27]. For example, Hanada et al. reported that the $\{332\}$ twin can produce high work hardening rate and further significantly improve the ductility of slip-dominated β-Ti alloys [19]. Min et al. found that $\{332\}$ twin combined with dislocation slip can effectively improve the yield strength and greatly enhance uniform elongation [24].

However, a lack of clear understanding of the origin and the mutual competitions of $\{112\}$, $\{332\}$, and other highly-indexed twins impedes the efforts to improve the mechanical properties of β-Ti alloys. Recently, many studies reported hierarchical twin structures, which are composed of multiple types of twinning modes with different volumetric ratios, at the early stage of $\{332\}$ twin formation. Mantri et al. observed a secondary $\{112\}$ twin inside $\{332\}$ twin by a tensile tested Ti-12 wt.% Mo alloy samples [28]. Sun et al. carried out experiments to show that both $\{112\}$ and $\{332\}$ twins are activated simultaneously in Ti–12 wt.% Mo alloy in the early deformation stage (uniaxial tensile loading) [17]. However, how to control the volume fraction of $\{112\}$ twin and $\{332\}$ twin in the hierarchical twin structure is still unclear. Current studies agree that twin system selection is controlled by the Schmid factor [8, 9, 29–31], but it is still unclear how materials properties (e.g., composition) and external conditions (e.g., temperature, engineering strain rate) affect the critical resolved shear stress for a particular twin mode. Meanwhile, there is a lack of quantitative investigations on the role of $\{112\}$ twin in the formation mechanism of the hierarchical twin structures and how these hierarchical twin structures further affect the mechanical behavior of β-Ti alloys. Thus, to fully understand the variation of deformation twin modes and the related impacts on the mechanical behavior of β-Ti alloys, it is critical to first uncover the physical mechanisms of the $\{112\}$ twin nucleation and early-stage growth kinetics in β-Ti alloys. These mechanisms may result in the rare appearances of $\{112\}$ twins and promote the alternative highly-indexed twins in β-Ti alloys depending on alloy compositions and deformation conditions.

In many BCC transition metals and alloys, $\{112\}$ twin nucleation and growth can be explained

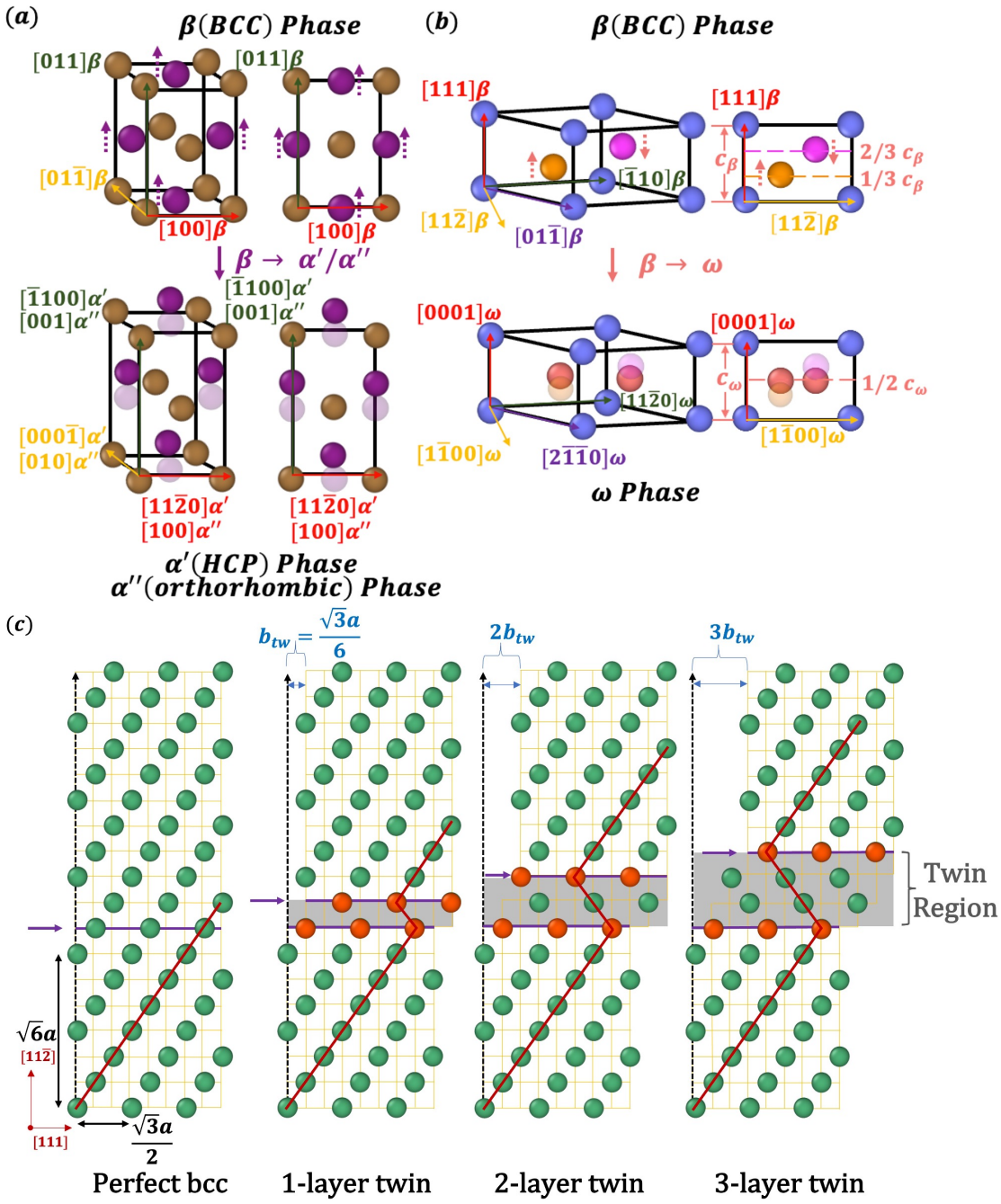

Figure 1: Illustrations of atomistic structures related to possible diffusionless phase transformation and twinning in BCC lattice. (a) Schematic draw for crystal structures of β (BCC), α' (HCP), α" (Orthorhombic) phases and the corresponding diffusionless transformation pathways. Brown and purple atoms are at A and B stacking of $\{01\bar{1}\}$ layers in BCC lattice, respectively. (b) The schematic draw for β to ω phase diffusionless transformation. Blue, orange, and magenta atoms are at A, B, and C stacking of $\{01\bar{1}\}$ layers in BCC lattice, respectively. Blue and rose atoms are at A and B stacking of (0001) layers in ω phase, respectively. (c) $\{112\}$ twin formation through a layer-by-layer twin dislocation slip mechanism. Grey shape indicates the $\{112\}$ twin region. Green and red atoms are in BCC lattice and at $\{112\}$ twin boundaries, respectively. Here a is the lattice constant and $b_{\text{tw}} = \frac{1}{6}\langle 111\rangle$ is the $\{112\}$ twin Burgers vector.

by the formation and glide of twin dislocations [32–35]. The first dislocation model for {112} twin in BCC metals is called the Cottrell–Bilby model [32], which proposed that a stress-assisted dissociation of a sessile $\frac{1}{2}\langle 111\rangle$ screw dislocations on {112} planes results in a $\frac{1}{3}\langle 112\rangle$ sessile and a $\frac{1}{6}\langle 111\rangle$ glissile partial dislocations, and the twin further nucleates from this monolayer fault nucleus. Later, it was realized that the dissociation process in the Cottrell–Bilby model is not energetically favourable [36]. Meanwhile, Mahajan et al. conducted experiments to prove that twins should be nucleated by screw dislocations [37]. Based on this observation, Sleeswy et al. modified the Cottrell–Bilby pole model and proposed that a {112} twin nucleus can be formed by dissociation of a $\frac{1}{2}\langle 111\rangle$ screw dislocation into three $\frac{1}{6}\langle 111\rangle$ partial dislocations located on {112} planes [36]. This model is widely accepted and the formation of twin embryos can be achieved by the glide of $\frac{1}{6}\langle 111\rangle$ partial dislocations on adjacent {112} planes under applied shear stress to generate {112} atomic layer faults [38,39]. Furthermore, Vitek confirmed that in order to form a metastable {112} twin embryo, the minimum number of {112} atomic layer faults should be three [40]. Once the twin embryo is stabilized, it can further grow through a layer-by-layer mechanism by slipping more {112} planes along the $\langle 111\rangle$ direction [41]. The corresponding twin growth process is illustrated in Figure 1 (c). Ogata et al. used DFT calculations to evaluate {112} twin embryos for BCC Mo metals by calculating the twinning energy landscape, suggesting that Mo twin can grow in a layer-by-layer fashion after the twin embryo reaches five {112} layers [42]. Ojha et al. adopted similar theoretical methods and further provided both computational and experimental results for twin embryos of other metals and alloys, e.g., Fe, V, Nb, Ta, W, Fe-Si alloys, Fe-Ni alloys, and Fe-V alloys, showing the minimum thickness of twin embryos indeed changing with alloy types and compositions [43].

Structures and growth kinetics of {112} twins in β-Ti alloys are more complex than those in other BCC transition metals and alloys. The local stress and strain accumulated at twin boundaries can activate the metastable phase transformations [16], which can play an important role in the nucleation and growth of {112} twins. It is widely acknowledged that β to ω phase transformation is activated at {112} twin boundaries [14,16,44–54]. Recently, many studies indicate that reversible phase transformations between β and ω phases have a close relationship with {112} twin nucleation and growth [14,44,46,50], but they are still in a debate on the detailed mechanisms. Wu et al. proposed that ω phase can promote {112} twin formation and growth in β-Ti alloys. They suggested that switch between β phase and ω phase could be the driving force for {112} twin nucleation and growth [46], since they observed {112} twins nucleate and grow inside the nanoscale ω phase in Ti-30Nb-3Pd (wt.%) (VEC=4.275) alloy. Meanwhile, they argued that structurally ω phase has an equal probability to transfer back to BCC matrix or BCC twin, indicating that ω phase can serve as an intermediate state for twin growth. However, Chen et al. [45] argued that ω may not promote {112} growth, and the probability of transformation of ω phase to BCC twin is less than 0.5 because distorted ω phase prefers to transform back to the BCC matrix rather than to BCC twin. Moreover, Wu et al. observe a high density of ω phases in Ti-30Nb (wt.%) (VEC=4.18) after quenching from solid-solution treatment condition at 900 °C for 1h but no {112} twins can be found [46], which suggests that ω phase does not promote {112} formation and growth in this alloy.

To reconcile the above debates, the aim of this study is to enhance our understanding of how diffusionless phase transformations affect the stability and growth kinetics of {112} twin embryos in

β-Ti alloys. To achieve this goal, we employ both density functional theory (DFT) calculations and atomistic simulations based on classical interatomic potentials to determine the stability of twin configurations in various compositions and elements. Additionally, we investigate the growth kinetics of stable twin embryos under applied shear stress on {112} twin planes in β-Ti alloys at different temperatures using atomistic simulations. Both DFT and atomistic simulation results demonstrate that, as the valence electron concentration (VEC) of Ti alloys decreases with varying alloy compositions, the $\beta \rightarrow \omega$ phase transformations at {112} twin boundaries increase the critical thickness of {112} layers as stable twin embryos, possibly raising energy barriers of {112} twin nucleation events.

In addition, our atomistic simulations show that, as the thermodynamic stability of β phase is reduced as the VEC and/or temperature is below critical values ($\sim$4.25 e/a at 300 K), the applied shear stress that should drive the {112} twin growth can result in β twin $\rightarrow \alpha$'/α" $\rightarrow \beta$ matrix phase transformations inside the existing twin embryo and ω phases at the twin boundaries impede the twin boundary migration simultaneously, leading to the detwinning behavior to eliminate the {112} twin embryos. When the VEC value increases gradually at a constant temperature (300 K), the applied shear stress can drive the normal {112} twin growth through twin boundary migrations, but ω phases at {112} twin boundaries can first reduce and then increase the required stress for the growth of the existing stable twin embryo; the minimum required stress for {112} twin embryo growth is observed in a Ti-Nb alloy with an intermediate VEC value ($\sim$4.34 e/a at 300 K). We explain the changes of ω effects on {112} twin embryo growth kinetics by using the free energy landscape variations of β matrix $\rightarrow \omega$ phase $\rightarrow \beta$ twin phase transformations. These findings are useful for understanding the thermodynamic and kinetic factors that result in the rare appearances of {112} twins in many β-Ti alloys. These thermodynamic and kinetic factors can provide effective strategies to manipulate the chemical compositions to tune the {112} twin activities. Similar investigations on the correlations between metastable phase stability and highly indexed twinning modes will be conducted in the future. The generated knowledge together will be utilized to tune the types and ratios of deformation twin modes to improve the mechanical properties of β-Ti alloys.

2 Methods

2.1 DFT calculations

Three steps were applied to construct the supercells of β-Ti alloys that contain {112} twin embryos with different thicknesses for investigations of their atomistic structures and energetic stability at 0K. In the first step, we constructed 108-atoms supercells in perfect BCC lattice with orthogonal basis vectors, namely $\frac{3}{2}[111]\times2[\bar{1}10]\times3[11\bar{2}]$, based on the conventional BCC lattice vectors. There are 18 atomic layers along $[11\bar{2}]$ direction, so each {112} layer contains 6 atoms. Meanwhile, the special quasi-random structure (SQS) method was employed to generate lattice occupations of different chemical elements at given compositions [55, 56]. This method optimizes the correlation function of lattice occupations in finite periodic supercells for simulations of random solid-solution alloys. Figure 2 (a) shows an example of such an SQS supercell for Ti_3Nb alloy in a perfect BCC lattice before structural relaxation by DFT calculations. For all 18 $(11\bar{2})$ layers in a supercell, we assigned a number from 1 to 18 as its layer index from the bottom to the top of the supercell along $[11\bar{2}]$ direction plotted in

Figure 2 (a). We can also shift one atomic $(11\bar{2})$ plane along the $[11\bar{2}]$ direction periodically to generate a "new" supercell with the same SQS-optimized lattice occupations but different layer index numbers (an original Layer n becomes a new Layer $n+1$ (or Layer $n-17$ due to the periodic condition), where n is an integer from 1 to 18). For each SQS-optimized lattice configuration, we can generate 18 supercells with different layer indexes. Correspondingly, we can deform all these supercells to generate twin layers at the same locations (between Layer i and Layer j, where i and j are integers between 1 and 18) in the same SQS-optimized supercell but with different local alloy compositions and occupations.

In the second step, we generated an n-layer $\{112\}$ twin embryo in the middle of the supercell based on a layer-by-layer mechanism [40]. Starting from Layer $9-\frac{n}{2}$ (or Layer $9-\frac{n+1}{2}$ if n is an odd integer), we shifted the upper $(11\bar{2})$ planes along the [111] direction by the length of one twin Burgers vector b_{tw}, which is equivalent to $\frac{1}{6}[111]$, then we shifted all the upper $(11\bar{2})$ planes above Layer $10-\frac{n}{2}$ (or Layer $10-\frac{n+1}{2}$ if n is an odd integer) by two b_{tw}. We repeated this layer-by-layer process until all the upper $(11\bar{2})$ planes above Layer $9+\frac{n}{2}$ (or Layer $9+\frac{n-1}{2}$ if n is an odd integer) by n b_{tw}, Thus, a n-layer twin growth fault was created at the middle of the supercell on successive $(11\bar{2})$ planes as the twin embryo region marked in grey color in Figure 1 (c). However, there is still one twin growth fault between the top and bottom layers on the boundary of the supercell along $[11\bar{2}]$ direction. So our third step was to change the supercell by tilting its $[11\bar{2}]$ axis along [111] direction by n b_{tw} to avoid the mismatch at the supercell boundary.

In this study, we generate three different types of twinned supercells with 3, 6, and 9 $(11\bar{2})$ layers of twin embryos in the middle of each supercell. We chose these numbers of layers because Vitek suggested that the minimum number of $\{112\}$ layer faults to form a metastable $\{112\}$ twin embryo should be three in pure BCC metals [40]; We also preferred to choose to tilt $3m$ b_{tw} (m is an integer) of the $[11\bar{2}]$ supercell axis since $3m$ b_{tw} equal to m full Burgers vector in a perfect BCC lattice. The final supercells with these twin embryos are shown in Figure 2 (c), (d), and (e) for 3, 6, and 9 $(11\bar{2})$ layers of twin embryos, respectively. We also provide the schematic draw of this three-step supercell construction process in Supplemental Section S1. In addition, for each SQS-optimized lattice occupation of a given alloy composition, 18 different configurations of n-layer twin embryo were generated by using all 18 supercells with different layer indexes as mentioned in the first step. Thus, each n-layer twin embryo has different local alloy compositions and occupations, and the average concentrations of all 18 n-layer twin embryos are guaranteed to be equal to the alloy composition in its perfect BCC lattice.

All DFT calculations were performed using the Vienna Ab Initio Simulation Package (VASP) software [57,58]. We performed Brillouin zone (BZ) k-point sampling using the Γ-centered algorithm with 3×3×2 grids, with a first-order Methfessel-Paxton smearing of 0.2 eV for Brillouin zone integration [59]. Pseudopotentials based on the projector augmented wave (PAW) method were employed for the elemental constituents, with the generalized gradient approximation (GGA) of Perdew-Burke-Ernzerhof (PBE) for exchange-correlation energy functional [57,60–62]. The electronic configurations of pseudopotentials for Ti, Nb, V, and Mo were Ti_pv, Nb_sv, V_pv, and Mo_pv, respectively. The corresponding electron configuration is $([\mathrm{Ar}])3s^2 3p^6 3d^2$, $([\mathrm{Kr}])4s^2 4p^6 4d^3 5s^2$, $([\mathrm{Ar}])3s^2 3p^6 3d^2$, $([\mathrm{Kr}])4s^6 4d^4 5s^2$, respectively. We set the energy convergence threshold for all calculations at 10^{-5} eV and used a plane-wave cutoff energy of 350 eV. The methods used for data visualization and analyses

for DFT results on structures and energies are from Seaborn, a Python data visualization library [63].

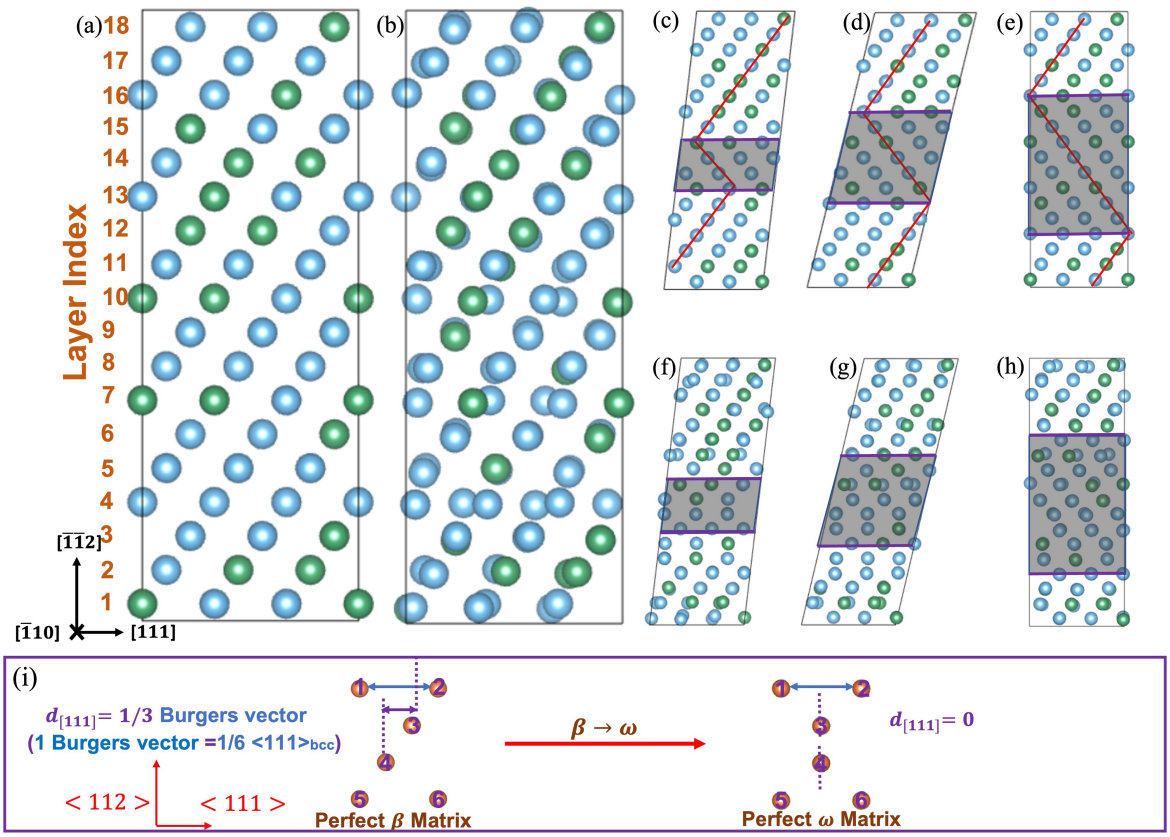

Figure 2: Illustrations of {112} twin embryo structures in a 108-atom Ti_3Nb supercell ((a)-(h)) and quantitative analyses for β (BCC) to ω (hexagonal) phase transformation in DFT-relaxed supercell based on values of a structural descriptor((i)). (a), (c), (d), and (e) show a perfect 18-layer BCC matrix, 3-layer twin embryo, 6-layer twin embryo, and 9-layer twin embryo in unrelaxed structures, respectively; (b) and (f)-(h) are the corresponding DFT-relaxed structures. The coordination system is the same as Figure 1 (c). Numbers at the left side of (a) are the layer indexes for the atomic layer along the $[11\bar{2}]_\beta$ direction. Red lines in (c), (d), and (e) indicate the crystal orientations. Grey shapes in (c) to (h) indicate the {112} twin embryo region. Blue and green atoms are Ti and Nb, respectively. (i) Explanations of the definition of a structural descriptor $d_{[111]}$ to distinguish between individual atoms in β phase and those in ω phase quantitatively. $d_{[111]}$ is the shortest distance projection along $[111]_\beta$ direction between one atom and its first-nearest neighbors of all the atoms in the supercell defined in (a).

2.2 Choices of alloy compositions based on phase stability

In this study, we investigated how {112} twin boundaries may induce $\beta \rightarrow \omega$ diffusionless phase transformation and how ω phase could further affect the {112} twin embryo stability and growth kinetics. Thus, we should investigate the composition region where β phase is thermodynamically (meta)stable so that the $\beta \rightarrow \omega$ transformation would not spontaneously occur. Meanwhile, phase stability in Ti alloys is highly related to VEC: $\beta \rightarrow \omega$ transformation can be easily induced by local chemical concentration fluctuations and local lattice distortion when the average VEC is low (close

to 4.0 e/a, where e/a means electron per atom) [14,64]. Here we define the VEC for pure Ti, pure Nb, pure V, and pure Mo as 4.0, 5.0, 5.0, and 6.0 e/a, respectively, although some core electrons of these chemical elements are included in their electronic configurations of pseudopotentials. We first generated around 100 supercells in perfect BCC lattice with different VEC values ranging from 4.0625 to 4.5 e/a. As we show in Figure 1 (b), β to ω phase transformation is achieved by atomic displacements along one of preferred $\langle 111 \rangle_\beta$ directions. Meanwhile, if no external stress/strain is applied and ω phase forms after DFT relaxations, the preferred $\langle 111 \rangle_\beta$ directions can be random locally. To quantify the displacement direction preference and further evaluate the ratio of ω phase in the DFT-relaxed supercell, we employed the approach developed by Ikeda et al. [64]. In each relaxed supercell, we first calculated and averaged all atomistic displacements from the perfect lattice sites projected along four distinct directions: $[111]_\beta$, $[1\bar{1}\bar{1}]_\beta$,$[\bar{1}\bar{1}1]_\beta$, and $[\bar{1}1\bar{1}]_\beta$, respectively. The averaged displacement magnitudes of four $\langle 111 \rangle_\beta$ directions are normalized by c_ω, which is the distance between the first nearest neighbors in the corresponding BCC lattice. Secondly, the four averaged displacement magnitudes along four $\langle 111 \rangle_\beta$ directions are sorted as P_1 ,P_2, P_3, and P_4 in the order of decreasing magnitudes, respectively. Thirdly, the structural descriptor P_1-P_2 is defined as the value to quantify the ratio of ω phase in the relaxed supercell. If P_1-P_2 of the supercell is smaller than 0.04 c_ω, this supercell is regarded to stay the in BCC lattice from the statistically average aspect [64]. Otherwise, the relaxed supercell is considered to be transferred into ω phase. The calculated P_1-P_2 for all the supercells are shown in Section S2.

Based on the scatter plot presented in Section S2, when VEC is equal or greater than 4.25 e/a for a series of Ti alloys, the BCC lattice can be preserved and does not spontaneously transfer to ω phase after DFT relaxations. These results of the critical VEC value (4.25 e/a) are generally consistent with previous Ikeda's results [64]. So we only investigated the supercells with VEC no less than 4.25. We conducted DFT calculations to investigate the atomic configurations and stability of twin embryos without any external stress at zero K. Thus, the supercells for DFT calculations of twin embryo stability in Section 2.1 were made up of six different compositions: $Ti_{81}Nb_{27}$ (VEC=4.25 e/a), $Ti_{81}V_{27}$ (VEC=4.25 e/a), $Ti_{72}Nb_{36}$ (VEC = 4.33 e/a), $Ti_{72}Nb_{18}V_{18}$ (VEC = 4.33 e/a), $Ti_{81}Mo_{27}$ (VEC = 4.5 e/a), and $Ti_{72}Nb_{18}Mo_{18}$ (VEC = 4.5 e/a). Hence average VEC values for the alloys we constructed here range from 4.25 to 4.5 e/a. However, it should be emphasized that the critical VEC value for ω phase should depend on both types of chemical elements and temperatures. In the following sections, we ignore the unit of e/a for VEC values for convenience.

2.3 ω phase identification in twinned supercells

To quantitatively identify the ω phase formed after the DFT relaxation in the twinned supercells, we propose a structural descriptor $d_{[111]}$ to distinguish the phases (ω and β) for different twinned supercells. Here we do not employ P_1-P_2 illustrated in the previous section to identify the ω phase for the following reasons [64]. β to ω phase transformation has the preference of atomic displacement direction in twinned supercells constructed following the orientations plotted in Figure 2. On the other hand, the descriptor of P_1-P_2 is only suitable for the bulk β phase and it fails to work for those twinned supercells. Based on the orientations of supercells defined in Figure 2, the smallest distance projected along $[111]_\beta$ between one atom and its nearest-neighbor atoms on the adjacent $(11\bar{2})$ layers

is $\frac{1}{3}$ of $\frac{1}{2}[111]_\beta$ in β phase. However, this projection distance is 0 in a perfect ω phase. The detailed illustration is shown in Figure 2 (i).

2.4 MD calculations

Molecular dynamics (MD) simulations were performed by Large-scale Atomic/Molecular Massively Parallel Simulator (LAMMPS) [65]to investigate Ti-Nb binary alloys using Modified Embedded Atom Method (MEAM) potential developed by Ehemann et al. [66]. As for the simulation box setting, 32400 atoms were included in a supercell with basis vectors of $15[111]\times20[\bar{1}10]\times9[11\bar{2}]$ in the unit of conventional BCC lattice vectors. For examinations of twin embryo stability at room temperature, MD simulations were performed on the supercells at a constant temperature of 300K under the isothermal-isobaric (NPT) ensemble ($P = 0$) for 200 ps. The time step was set to be 1 fs. The energy and structure of the system were calculated every 1 ps. For chemical compositions of Ti alloys, we chose five different compositions: Ti_3Nb (VEC = 4.25), Ti_2Nb (VEC =4.33), TiNb (VEC = 4.5), $TiNb_3$ (VEC = 4.75), and pure Nb (VEC =5). Besides, each composition was applied to generate 4 different structures: perfect BCC, 3-layer twin embryo, 6-layer twin embryo, and 9-layer twin embryo, which are all consistent with the structures setting of DFT calculations plotted in Figure 2. Furthermore, we deformed the supercells that contain the stable twin embryos by applying shear stress with a constant engineering shear strain rate of 4×10^8 s^{-1} along [111] direction on $(11\bar{2})$ plane at 300 K. The time step for the deformation simulation was also 1 fs. An MD simulation of 30 ps at 300 K in an NPT ($P = 0$) ensemble was performed for equilibrium before each deformation operation. To analyze the atomistic structures generated by MD simulations, we used the polyhedral template matching (PTM) [67] and the grain segmentation method to identify BCC matrix, BCC twin, and α'/α" phase [68]. In addition, we also applied OVITO to visualize all the MD results [69].

2.5 Calculations of a twinning pathway through homogeneous displacements in Ti-Nb alloys

To evaluate the energy landscape for both the twinning and anti-twinning deformation that may occur to a pre-existing twin embryo observed in our MD simulations, we define a twinning pathway through homogeneous displacements between different parts of a crystal near an existing {112} twin boundary to generate a type of defects named as "twin growth faults" and calculate the related energy variations. The simulation box used for calculations of the twinning pathway and the related twin growth fault energies is shown in Figure 3 (a). Here, we construct an orthogonal supercell with basis vectors of $30[111]\times30[\bar{1}10]\times12[11\bar{2}]$ (72 atomic layers along $[11\bar{2}]$ direction) in the unit of conventional BCC lattice vectors. The supercell contains {112} twin boundary located in the middle (viewing along $[\bar{1}10]$ direction). The location of the initial twin boundary is marked in red dashed line. We use the Common Neighbor Analysis (CNA) method in OVITO [69–71] for phase identifications. Green and light brown atoms are both in the BCC phase; white atoms are at/near the twin boundary and are classified as the "Other" phase by the CNA method. Green atoms are in the same orientation as the BCC twin region in Figure 2 (c)-(e) while light brown atoms are in the same orientation as the BCC matrix in Figure 2 (c)-(e). The color correspondences (light brown color for the BCC matrix and

green color for the BCC twin) are consistent with the following sections of this paper.

To generate twin growth faults at the twin boundary, we displace the atoms in the BCC matrix (the upper crystal above the twin boundary) with certain fault displacements in the way of homogeneous displacements. Figure 3 (b) shows an example of the creation of a 2-layer twin growth fault. We shift the upper atomic layer adjacent to the twin boundary (the red dashed line) along [111] direction by the magnitude of $\lambda \times \frac{1}{2}[111]$ relative to the bottom crystal; we also shift all the upper layers (except the atomic layer that is adjacent to the twin boundary and is already shifted) along [111] direction with the magnitude of $2\lambda\times \frac{1}{2}[111]$ relative to the bottom crystal, where λ ranging from 0 to 1 in the interval of 0.01. So the maximum fault displacement is the length of one or two full Burgers vectors in BCC lattice (when λ approaches 1), which is the smallest unit length of structure periodicity along [111] direction in BCC lattice. The method of twin growth faults energy calculation is similar to the twinning pathway designed by Ogata et al. [42] and also recently applied by Gröger et al. [72] to investigate the energy landscape of deformation twinning in BCC metals. However, the difference is that the two-layer displacements were applied in a perfect BCC lattice to generate a two-layer stacking fault in previous studies [42,72], but we apply the two-layer homogeneous displacement mechanism near an existing {112} twin boundary in a bicrystal structure to simulate the twinning and anti-twinning deformation during the twin growth process. So the defects generated during this homogeneous displacement process are not simply stacking faults in a perfect crystal. Thus, we name this type of defect generated in Figure 3 (b) as "twin growth fault".

To calculate the energy profile along the twinning pathway by the twin growth fault generation, we use the conjugated gradient (CG) minimization method [73]. The relaxation convergence for force is 1×10^{-6} eV/Å and the energy tolerance is 1×10^{-6}. During the relaxation minimization, the bottom and top regions along $[11\bar{2}]$ direction in the supercell are frozen (grey regions in Figure 3) to ensure that only atoms near the twin boundary are included in the calculation and no energy contribution from extra surfaces. Meanwhile, the thicknesses of the frozen part should be large enough to avoid the interactions between movable atoms and atoms in the top/bottom frozen regions. As for the unfrozen part of the supercell, atoms are only relaxed along $[11\bar{2}]$ direction perpendicular to the $(11\bar{2})$ twin boundary plane after the homogeneous displacements are applied. Here, we define the energy of twin growth faults induced by homogeneous displacements, $\gamma^n_{\mathrm{TGF}}(\lambda)$, using Eq. 1 below:

$$\gamma^n_{\mathrm{TGF}}(\lambda) = \frac{E^n_\lambda - E_0}{A} \tag{1}$$

Here E^n_λ is the relaxed energy of the supercell that contains n-layer twin growth faults with the magnitude of $\lambda \times \frac{1}{2}[111]$ of homogeneous displacements as described in Figure 3(b) (Here $n = 2$). E_0 is the relaxed energy of the supercell without any twin growth faults. A is the area of one fault plane defined by the supercell size. In the following sections, we simplify the name of energy of the twin growth fault as γ_{TGF} for convenience because we always study 2-layer twin growth faults. A key reason for presenting the results of 2-layer twin growth faults is that the energy barriers in 2-layer twin growth faults are smaller than those in other n-layer (n= 1,2 and 3) twin growth faults cases based on our calculations. Similarly, 2-layer stacking faults are also found to be the pathway with the minimum energy barriers for the stacking fault generation in many BCC transition metals (Nb, Ta, etc.) according to a recent computational study by Gröger et al. [72]

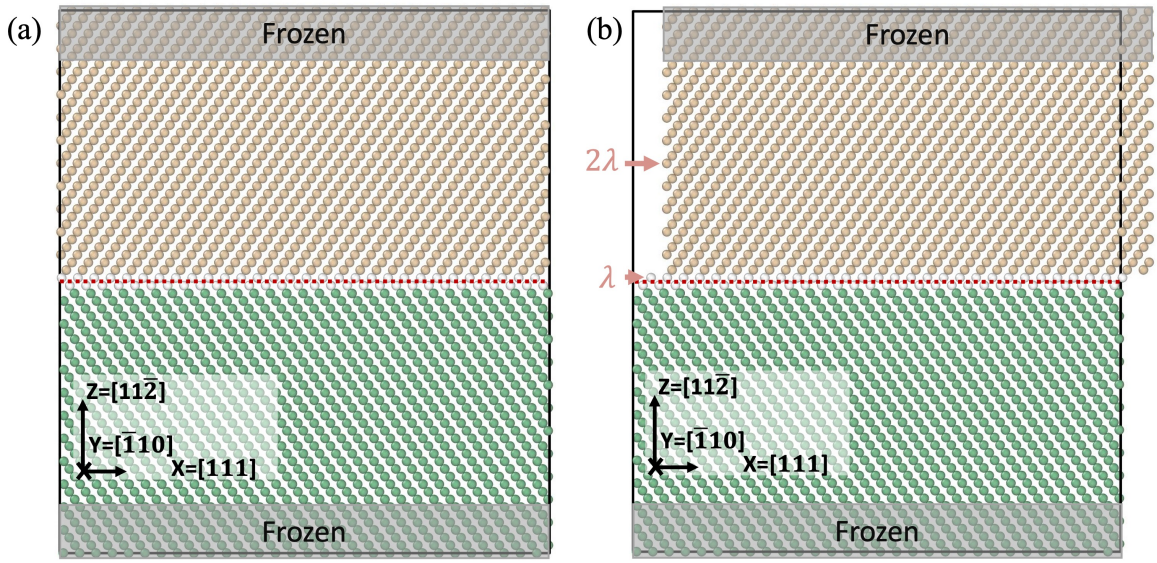

Figure 3: Schematic illustration for a twin pathway through homogeneous displacement mechanism near an existing {112} twin boundary in a bicrystal structure. Here we present the twin structure of pure Nb as an example. (a) is the bicrystal structure that contains a $(11\bar{2})$ twin boundary in the middle, viewing along $[\,1\bar{1}0]$ direction. A red dashed line is plotted to mark the location of the initial twin boundary. We use the Common Neighbor Analysis (CNA) method in OVITO [69–71] to identify phases. Green and light brown atoms are both in the BCC phase; white atoms are at/near the twin boundary and are classified as the "Other" phase by the CNA method. Green atoms are in the same orientation as the BCC twin region in Figure 2 (c)-(e) while light brown atoms are in the same orientation as the BCC matrix in Figure 2 (c)-(e). The color correspondences are consistent with the following sections of this paper. (b) is the bicrystal structure under a twinning pathway created by homogeneous displacements between different parts of the upper crystal. Atoms in the first $(11\bar{2})$ atomic layer adjacent to the twin boundary shift together by $\lambda \times \frac{1}{2}[111]]$ relative to the lower crystal. Atoms above the first $(11\bar{2})$ atomic layer adjacent to the twin boundary shift together by $2\lambda \times \frac{1}{2}[111]$ relative to the lower crystal. λ ranges from 0 to 1 at the interval of 0.01. Atoms in grey shade regions are fixed during the energy minimization and the atoms out of the grey regions are only allowed to be relaxed in the Z direction normal to $(11\bar{2})$.

2.6 Experimental characterizations of twin boundary structures

To verify the structures of twin boundaries obtained from the above atomistic simulations, the atom configurations at the $\{112\}\langle 11\bar{1}\rangle$ type twin boundary were characterized in the β Ti-24Nb-4Zr-8Sn (wt. %, Ti-2448) alloy. Since we want to investigate how $\{112\}$ twin-induced ω phase affects the $\{112\}$ stability and configurations and so pre-existing athermal ω phase should be avoided. Here, we carefully choose this composition and the addictive Zr and Sn can help suppress the quenched-in athermal ω phase [74–76]. We use conventional transmission electron microscopy (TEM) and aberration-corrected z-contrast high angle annular dark field-scanning transmission electron microscopy (HAADF-STEM) for characterization. Ti-2448 was β solution treated at 1000°C for 30 min followed by water quenching to room temperature, and then cold-rolled by 20% reduction in thickness. The β solution treated and cold rolled Ti-2448 was cross-sectioned, mounted, and ground for characterization following conventional routes. Site-specific TEM lift-out lamella for TEM and HAADF-STEM was prepared across the $\{112\}$ twin boundary using Thermo Scientific Scios 2 dual-beam focus ion beam (DB-FIB), and further cleaned using Fischione 1040 nanomill. Conventional TEM was performed using FEI Talos F200s transmission electron microscope at 200kV, and atomic resolution HAADF-STEM imaging was performed using aberration-corrected Thermo Scientific Themis Z scanning transmission electron microscope at 300kV.

3 Results

3.1 Structures and stability of {112} twin embryos at 0K

Examples of atomistic structures in DFT-relaxed supercells are shown in Figure 2 (b), (f), (g), and (h), respectively, for the perfect BCC lattice and twin embryos of Ti_3Nb (108-atom supercell, VEC = 4.25). More snapshots of fully relaxed twin embryo structures for Ti_3Nb (VEC=4.25) and Ti_3Mo (VEC=4.5) can be found in Section S3. By comparing Figure 2 (a) and (b), we do not observe a perfect ω matrix in the relaxed supercell, which initially was in an ideal BCC lattice. This is consistent with the conclusion that spontaneously β to ω phase transformation hardly occurs when VEC is equal to or greater than 4.25, as discussed in Section 2.2. However, in supercells that contain twin embryos before relaxations, local atomistic structures with the structural features of ω phase can be identified at locations where twin embryos were generated. The structural features for the atomistic structure of ω phase are clearly shown in Figure 1 (b). Generally, if two adjacent atoms on two nearest neighbor $(11\bar{2})$ layers align in a line parallel to $[11\bar{2}]$ from the view of $[\bar{1}10]$ direction in a relaxed supercell, we can regard the local atomistic structures of these two atoms have the structural features of ω phase. When the number of $(11\bar{2})$ layers of the original twin embryo in the unrelaxed structure equals 3 or 6, most atoms in the twin regions (grey shape areas in Figure 2 (f) and (g)) have the structural features of ω phase by aligning to adjacent atoms along $[11\bar{2}]$ direction. Even when the number of $(11\bar{2})$ layers of the original twin embryo increases to 9, a large portion of atoms in the twin region (grey shape areas in Figure 2 (h)) still have the structural features of ω phase. However, when VEC increases to 4.5, the structural features of ω phase are hardly observed in the relaxed supercells. The snapshots of relaxed supercells (VEC = 4.5 cases) are shown in Supplementary Section S3.

We also quantitatively estimated the energy costs of these twin embryos in all the DFT relaxed supercells by using twin boundary (TB) energy γ_{TB} defined as the follow [77]:

$$\gamma_{\mathrm{TB}} = \frac{E_{\mathrm{twin}} - E_{\mathrm{perfect}}}{2A} \tag{2}$$

Here, E_{twin} is the energy of a relaxed twinned supercell, E_{perfect} is the energy of the corresponding relaxed supercell in the perfect BCC lattice, and A here represents the supercell area parallel to $(11\bar{2})$ twin boundary plane. Typically, γ_{TB} is greater than 0 and this parameter can indicate the energy cost to form a twin embryo. The calculated γ_{TB} values for different Ti alloys are plotted in Figure 4. The "violin" plots here are implemented by the Python package from Seaborn [63]. Each sub-figure in Figure 4 contains γ_{TB} calculated by using all the fully relaxed twinned supercells at a given composition (indicated at the top of each sub-figure).

As we discussed in Section 2.1, we generated 18 different supercells for each SQS-optimized lattice occupation of a given composition with a fixed number of twin layers in the middle of the supercell. Therefore, in each sub-figure of Figure 4, each column has 18 different data points, each of which corresponds to different local chemical compositions and lattice occupations in an alloy with the same average chemical composition. These data points are marked as black dots in the middle of each "violin" graph. Meanwhile, the width of the "violin" graph features a kernel density estimation of the data distribution. In this case, the widest location is where the most data is distributed. The dots linked by solid lines mark the location where the mean value of γ_{TB} distribution for the corresponding alloy composition.

Clearly shown by different alloy compositions in Figure 4, the average γ_{TB} increases as the VEC increases. This trend coincides with the fact that the β phase becomes stable relative to other phases (α', α", and ω) as the VEC increases [14, 64], so there should be less energetic driving forces of spontaneous β to ω phase transformation at twin boundaries. In addition, as for γ_{TB} distribution of different twinned supercells for each composition, especially when VEC is equal or greater than 4.33, we can see that the γ_{TB} variation becomes smaller as the number of $(11\bar{2})$ layer in the twin embryo increases. This indicates that a 3-layer twin embryo may not be stable and spontaneously disappear by diffusionless transformation. This is consistent with the observations of atomistic structures in Supplementary Section S3. For example, when VEC = 4.5, ω phase can still be observed in the configurations of 3-layer twin cases, while ω phase totally disappeared when $(11\bar{2})$ layer of the twin embryo increases to 6.

Moreover, γ_{TB} distributions for two alloy compositions of VEC equal to 4.25 (Figure 4 (a) and (d)) are mainly distributed at values that close or even less than 0. This indicates that the initially constructed twin embryos spontaneously induce a large portion of β phase in both the matrix and twin regions transforming into a lower energy state, more specifically, ω phase depending on the local chemical compositions. Even a 9-layer twin embryo plotted in Figure 4 (a) and (d) is not thick enough to survive for low VEC cases because the calculated γ_{TB} are still close to 0. Compared with higher VEC cases, we can conclude that for β-Ti alloys, the existing {112} twin embryos can induce the β to ω phase transformation depending on both the average alloy compositions (VEC) and the local lattice occupations, and vice versa, twin-induced ω phase impede the formation of stable twin embryos with

a small number of $(11\bar{2})$ layers.

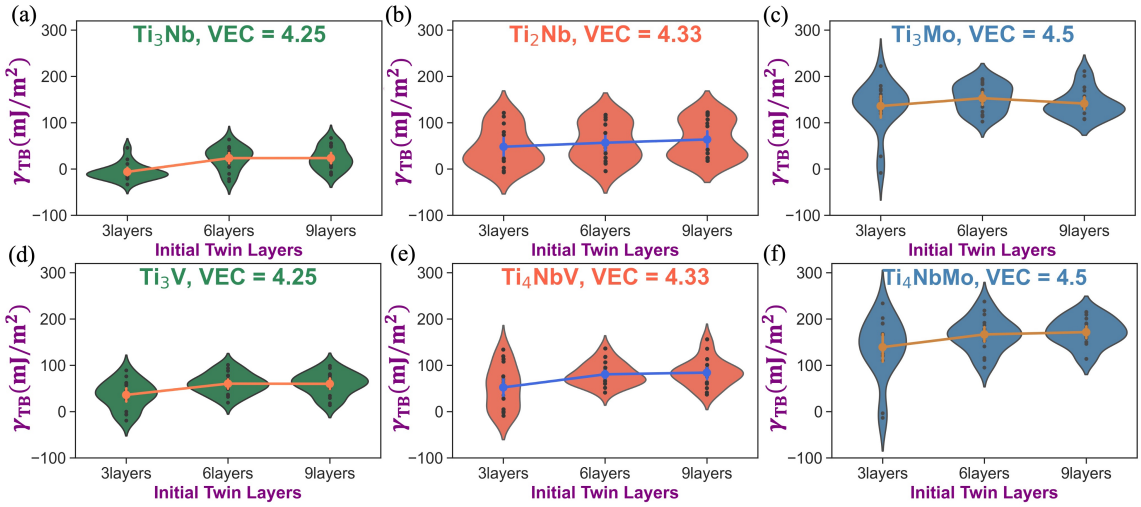

Figure 4: Twin boundary energy γ_{TB} defined in Equation 2 vs. the number of $(11\bar{2})$ layers of twin embryos for alloys with different VEC values. All cases were calculated by DFT using a supercell of 108 atoms plotted in Figure 2 (a). For each type of twin embryo structure at a given alloy composition, there are 18 possible cases to locate the twin embryo with different $(11\bar{2})$ layer indexes plotted in Figure 2 (a). So the "violin" plots of these 18 data points are used to illustrate the distribution and the mean value of γ_{TB} for each twin embryo structure at a given alloy composition. The detailed alloy compositions and the corresponding VEC values are shown at the top of each subfigure.

To confirm our conclusion on the quantitative correlation between twin embryo stability and phase stability, we employ the structure descriptor $d_{[111]}$ defined in Figure 2 (i) to distinguish atoms in ω phases and those in β phases. Here, We calculate the $d_{[111]}$ for all atoms in all supercells we generated so far. The histogram plots of $d_{[111]}$ for all atoms in different supercells are shown in Figure 5. Because all the supercells contain 108 atoms and there are 18 different atomic configurations for each composition with a given number of twin layers, each subfigure in Figure 5 is the histogram for the $d_{[111]}$ values of $18\times108 = 1944$ atoms (except those in Figure 5(a) and (e) for the perfect BCC lattices with twin embryos, which are histograms for the $d_{[111]}$ values of 108 atoms).

As explained in Figure 2 (i) and Section 2.3, since the value of $d_{[111]}$ is normalized by the value of $\frac{1}{2}[111]_{\beta}$, so if the peak of the histogram is located at 0.333 and no data points drop at 0, then statistically we can claim that the corresponding supercells are in β phase with a BCC lattice and ω phase does not appear. If there is a peak in the histogram located at 0, there are a significant amount of local ω phases in these supercells. In Figure 5 (a)- (h), we present histograms for two compositions: Ti_3Nb (VEC=4.25) and Ti_3Mo (VEC=4.5). The histograms for the other compositions can be found in Supplementary Section S4. As far as Ti_3Mo is concerned (Figure 5 (e)-(h)), there are no evident peaks near $d_{[111]} = 0$ in neither perfect lattice nor twinned supercells. Nevertheless, we can still observe a small portion of data points near the $d_{[111]} = 0$ region for 3-twin supercells (Figure 5 (f)). This is consistent with the energy data shown in Figure 4 (f), where we can see a large variation of γ_{TB} distribution for those 3-layer twin supercells. This indicates that the 3-layer twin embryo is not thick enough to stabilize for Ti_3Mo and collapses to ω phase. Meanwhile, as for other supercells for Ti_3Mo,

there are almost no data points less than 0.1. In contrast, when VEC = 4.25 (Figure 5 (a)-(d)), there are two comparable peaks for all the supercells except no-twin lattices: one is near $d_{[111]} = 0$ and the other one is near $d_{[111]} \approx 0.3$, suggesting that a large portion of β phase can transform to ω phase because of the low stability of β phase when the VEC value is low. Compared to the perfect lattice in Figure 5 (a), the peaks near $d_{[111]} = 0$ increase significantly for the twinned supercells in Figure 5 (b)-(d)), suggesting the introductions of twin embryo enhance $\beta \rightarrow \omega$ transformation remarkably. In addition, the case of the 9-layer twin embryo in Figure 5 (d) still has slightly stronger peaks near the $d_{[111]} = 0$ region compared with the case of 6-layer twin embryo in Figure 5 (c), suggesting that the twin embryos are still unstable when there are 9 $(11\bar{2})$ layers in the twin region.

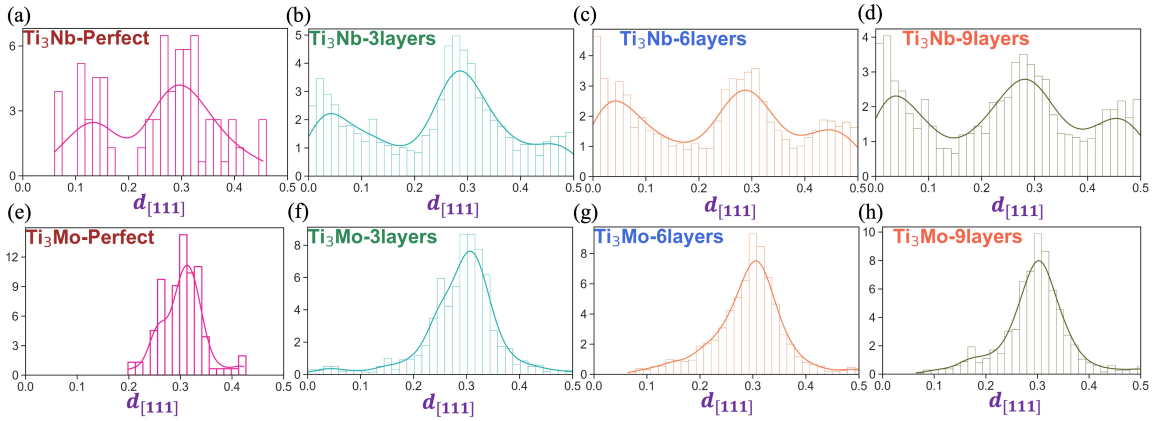

Figure 5: Histograms of $d_{[111]}$ values (normalized in the unit of the length of $\frac{1}{2}[111]_\beta$) for DFT-relaxed supercells of different alloy compositions and twin embryo structures. From left to right the subfigures in each row are for the perfect BCC matrix, 3-layer twin, 6-layer twin, and 9-layer twin embryo structure for a specific composition, respectively. (a)-(d) are for Ti_3Nb (VEC=4.25); (e)-(h) are for Ti_3Mo (VEC=4.5).

To conclude, both our energetic descriptor (γ_{TB}) and structural descriptor ($d_{[111]}$) indicate that the minimum thickness of a stable twin embryo varies with the VEC value of Ti alloy; a thicker twin embryo is required for be stable in β-Ti alloy a lower VEC; {112} twin boundaries can induce the β to ω phase transformation at low VEC and thus increase the difficulty of forming a stable twin embryo. However, these DFT supercell sizes are still too small to include the effects of local concentration fluctuations, and we have not investigated the stability and growth kinetics of twin embryos at different temperatures under external loading conditions. These size/temperature effects and growth kinetics are discussed in the following sections.

3.2 Stability of {112} twin embryos at room temperature

First, we investigated the stability of twin embryos at room temperature based on MD simulations using Ti-Nb MEAM potential [66]. The MD settings are described in Section 2.4. The snapshots for supercells after 200 ps of MD simulations under the NPT ensemble ($P = 0$ and $T = 300$ K) are plotted in Figure 6. Subfigures in each column from left to right in Figure 6 stand for supercells that initially (before MD relaxations) have the perfect BCC lattice, 3-layer twin embryo, 6-layer twin embryo, and 9-layer twin embryo, respectively, in different alloy systems. The light brown color represents the BCC

matrix while the green color represents the BCC twin identified based on the Polyhedral Template Matching (PTM) method [67]. Figure 6 (a)-(d) show atomistic structures of the unrelaxed supercells for all the alloy cases, where twin embryos are always added to the middle of a supercell through a layer-by-layer mechanism, and all supercells are constructed in the same way as described in Section 2.1).

Figure 6 (e)-(h) are MD-relaxed supercells of Ti_3Nb (VEC=4.25). It clearly shows that both 3-layer and 6-layer twin embryos disappear while the 9-layer twin embryo survives after MD relaxations. In addition, the boundaries between twin and matrix regions in Figure 6 (h) are not as flat as those in the unrelaxed supercell in Figure 6 (d). Figure 6 (i)-(l) and Figure 6 (m)-(p) are MD-relaxed supercells of Ti_2Nb (VEC=4.33) and TiNb (VEC=4.5), respectively. For both alloy cases, 3-layer twin embryos disappear, but both 6-layer and 9-layer twin embryos survive after MD relations. In addition, twin boundaries in both the relaxed Ti_2Nb and TiNb become more flat compared to those of Ti_3Nb. Figure 6 (q)-(t) are MD-relaxed supercells of Pure Nb (VEC=5), where all twin embryos survive and all twin boundaries are almost as flat as those in the unrelaxed supercells. In summary, the critical thickness of a stable twin embryo increases as the VEC value decreases: 3 atomic layers for Pure Nb (VEC=5), 6 atomic layers for TiNb (VEC=4.5) and Ti_2Nb (VEC=4.33), 9 atomic layers for Ti_3Nb (VEC=4.25). This trend is also consistent with DFT results in Section 3.1: alloy compositions with low VEC values increase the difficulty of identifying stable twin embryos with BCC lattice due to the local $\beta \rightarrow \omega$ transformation. This transformation usually is intensified on twin boundaries. Thus, the ultra-thin twin embryos with two twin boundaries too close to each can not survive after MD relaxations because ω phases on two twin boundaries can interact with each other, transforming almost all atoms inside the twin region into ω phase.

To further confirm the effects of ω phases on twin embryo stability in these MD simulations, we applied quantitative methods to identify the ω phases on twin boundaries in the relaxed supercells that contain stable twin embryos with the minimum number of atomic layers (6 atomic layers for TiNb (VEC=4.5) and Ti_2Nb (VEC=4.33), 9 atomic layers for Ti_3Nb (VEC=4.25)). We employed the same descriptor $d_{[111]}$ defined in Figure 2 (i) to quantitatively define the extent of $\beta \rightarrow \omega$ transformation of each atom according to its first-nearest-neighbor environment in these selected supercells. In addition, for each relaxed supercell after MD simulations, we first run 10 steps of conjugated gradient (CG) minimization to remove the noises due to thermal vibrations [73]. Here, even though ω phases and α'/α" phase have some similarities viewing from $[\bar{1}10]$ direction (both of them have 0 projection distance of two adjacent $(11\bar{2})$ planes), occurrence of $\beta \rightarrow \alpha$'/α" phase needs external shear stresses [10] and α'/α" phase can not survive without external stresses. Hence, $d_{[111]}$ is still an efficient structural descriptor to identify ω phases in the supercells if they are free of external stresses. Figure 7 (a)-(c) are snapshots of some selected supercells after the CG minimization. We calculated $d_{[111]}$ for all the atoms in these supercells. Similar to the distribution shown in Figure 5, the $d_{[111]}$ values have a continuous distribution. In order to distinguish the local ω phase, here we assign two discrete values (0 and 1) to each atom based on the corresponding $d_{[111]}$. Value 0 indicates ω phase while 1 indicates β phase. If $d_{[111]}$ of the atom is less or equal to 0.1, then we assume this atom is in the ω phase. Otherwise, we treat the atom as β phase. Here, we make $d_{[111]} = 0.1$ as the cutoff value for phase identification is based on the histogram plot in Figure 5 (h). In 9-layer twinned supercells of Ti_3Mo

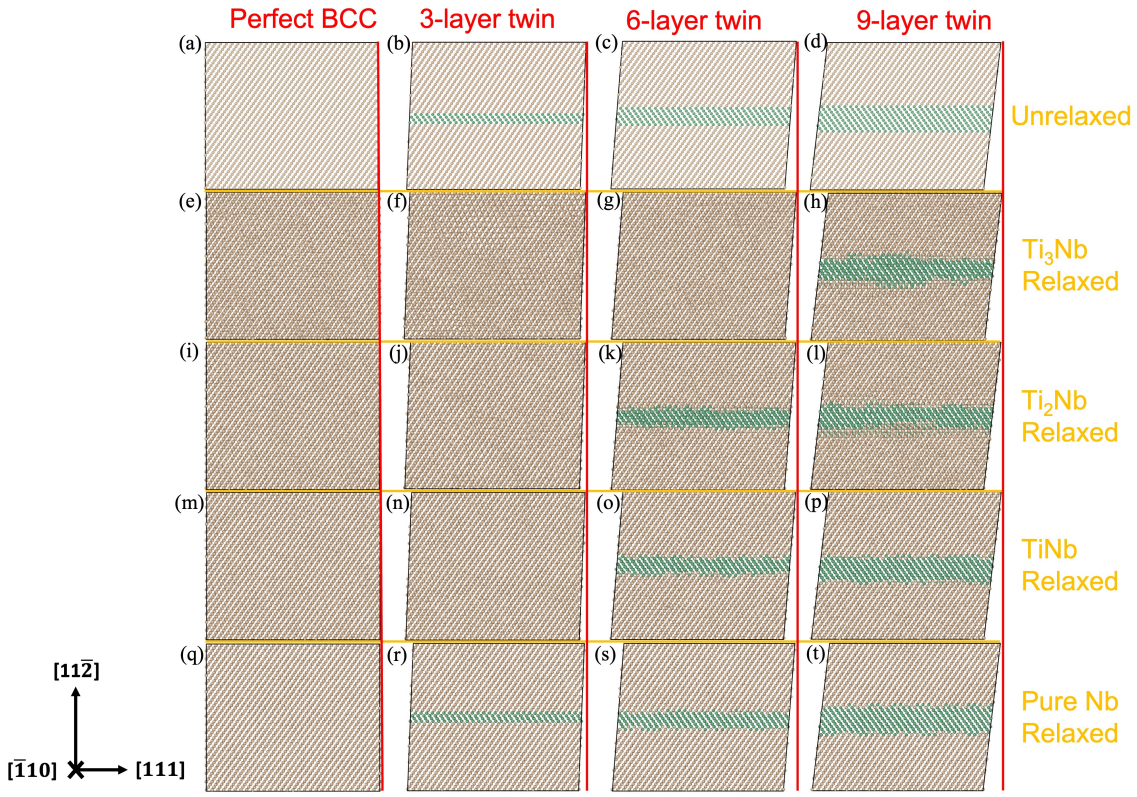

Figure 6: Configurations of {112} twin embryos in Ti-Nb alloys after MD simulations (200 ps and the NPT ensemble ($P = 0$ and $T = 300$ K)). Subfigures of each column from left to right are supercells that initially (before MD relaxations) have the perfect BCC lattice, 3-layer twin embryo, 6-layer twin embryo, and 9-layer twin embryo, respectively, in different alloys. Subfigures of each row are supercells for different alloys. (a)-(d): Unrelaxed supercells of all alloy cases before MD relaxations. (e)-(h): Relaxed Ti_3Nb supercells. (i)-(l): Relaxed Ti_2Nb supercells. (m)-(p): Relaxed TiNb supercells. (q)-(t): Relaxed pure Nb supercells. The light brown color represents the BCC matrix while the green color represents the BCC twin. Phase identification is conducted by Polyhedral template matching (PTM) [67] and phase variants identification (BCC matrix and BCC twin) is conducted by Grain segmentation method [68] in the current version of OVITO [69].

(VEC= 4.5), β phase should be stable, and {112} twin boundaries should not induce $\beta \rightarrow \omega$ phase transformations, so the corresponding 9-layer twin embryo supercells should do contain almost zero atoms with local atomistic structures with the structural features of ω phase. Also, we notice that there are almost no distributions of $d_{[111]}$ value less than 0.1 in Figure 5 (h). So 0.1 can be a valid and efficient cut-off to separate ω-like phase and β-like phase by considering the local atomistic structures. Here, we do not choose a histogram of perfect BCC lattice of Ti_3Mo as a reference to decide the cutoff value (in Figure 5 (e), there are almost no distributions of $d_{[111]}$ value less 0.2). The reason is that twin boundary structures can trigger local lattice distortion and change the value of $d_{[111]}$, so we should allow a large variation of $d_{[111]}$ values for atoms in β phase that contains twin boundaries.

Figure 7 (d)-(f) is the heatmap of supercells shown in Figure 7 in (a)-(c) based on assigned two-phase identification values of $d_{[111]}$. When VEC equals 4.25, we can see 4 to 5 layers of ω phases (marked in black color in Figure 7 (d)) stacking along the top and bottom twin boundaries (enclosed in red and green dashed lines). Also, the twin boundaries in Figure 7 (d) are not homogeneous and we can see some kinks and steps along the twin boundaries (marked in green color) due to the variations of ω phase locations. This is why the twin phase (green region) in Ti_3Nb shown in Figure 7 (a) are thick and rough compared with those in Ti_2Nb and TiNb shown in Figure 7 (b) and (c). The structural features are consistent with those observed in the aberration-corrected high-angle annular dark field scanning transmission electron microscopy (HAADF-STEM) images shown in Figure 7 (g) and (h). In Figure 7 (g), the twin boundaries are composed of stacked ω structures ranging from 2 to 4 atomic layers in thickness. These structures (both simulation results in Figure 7 (d) and experimental results in Figure 7 (g)) are also consistent with the findings in Section 3.1 that {112} twins activate the β to ω structural transformation. In addition, in Figure 7 (d), we can observe that a part of the twin regions is collapsed to a 4-layer of ω phase; we can also find some ω phases locate away from the twin embryo in Figure 7 (d). These features of ω phases distributions are because the local VEC is much less than 4.25 due to local concentration fluctuations and the original local β phase can spontaneously transfer to ω phase. When VEC increases in Figure 7 (e) and (f), the portion of atoms in ω phase (marked in black color) significantly reduces. We can see atoms in ω phase along each of the two twin boundaries form a thin and discontinuous line in Ti_2Nb (Figure 7 (e)), and almost no atoms in ω phase are identified in TiNb (Figure 7 (e)).

Meanwhile, we also measure the thicknesses of ω phase at twin boundaries in different VEC cases from this study and several published papers. [44–46, 54, 78–80], as shown in Figure 7 (i). The methods for thickness measurement are presented in Supplementary Section S5. Here, the solid circles in Figure 7 (i) represent the average thickness of local ω phases weighted by the lengths that parallel to the {112} twin planes. The error bars in solid lines are estimated by the weighted standard deviations of thicknesses of local ω phases in the experiment data. Generally, based on these experimental results, the average thicknesses of ω phase at twin boundaries decrease with the increase of VEC values of alloy compositions, especially in the Ti-Nb alloy system, which is consistent with our observations in our DFT calculations in Figure 5 and MD simulations Figure 7 (d)-(f). The only outlier is Ti-12Mo wt.% [44], which has a relatively small average thickness of ω phases at low VEC (VEC=4.13). This indicates that, although VEC is still the dominant factor, it is not the only factor that affects β to ω phase transformations at {112} twin boundaries. These factors may include oxygen effects

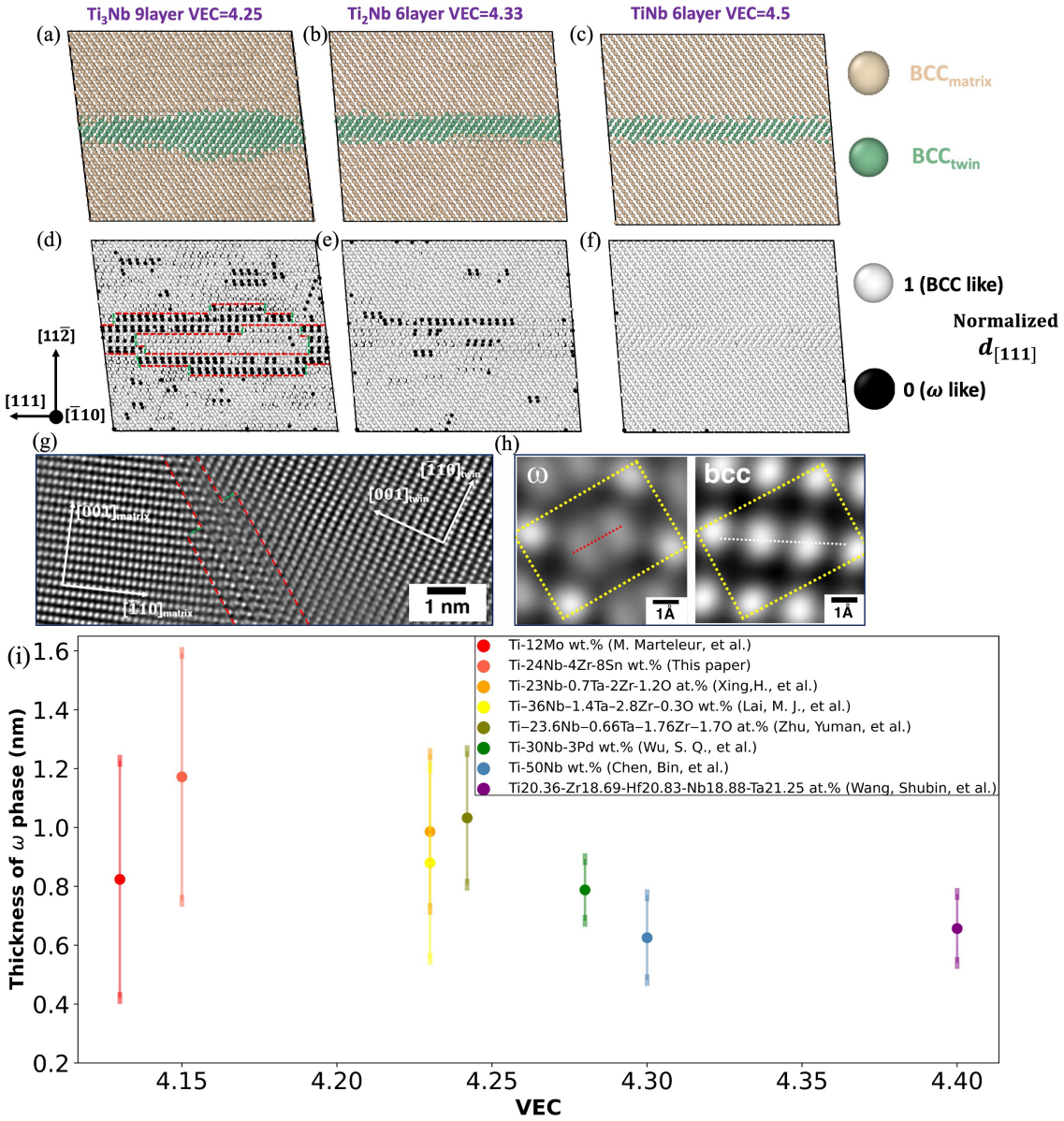

Figure 7: Detailed descriptions of twin boundary atomistic structures in both MD and experimental results. (a)-(c) are the snapshots of the relaxed supercells that contain stable twin embryos with the minimum number of atomic layers ((a) 9 atomic layers for Ti_3Nb (VEC=4.25), (b) 6 atomic layers for Ti_2Nb (VEC=4.33), and (c) 6 atomic layers for TiNb (VEC=4.5)). The brown color represents the BCC matrix while the green color represents the BCC twin. (d)-(f) are corresponding snapshots of (a)-(c) after phase identification (to distinguish ω phase and β (BCC) phase) by using the algorithm explained in Figure 2 (i) and Section 2.3. According to this algorithm, white color atoms are in the β phase and black atoms are in the ω phase. Both the top and bottom boundaries in (d) are enclosed by red and green dotted lines to highlight the thick twin boundary regions due to the formation of ω phase. Here red color lines mark the twin boundaries that are aligned with the twinning plane while green color lines mark the steps of the twin boundaries. (g) and (h) are aberration-corrected high-angle annular dark field scanning transmission electron microscopy (HAADF-STEM) images showing the hexagonal ω phase formed at {112} deformation twin boundary in the 20% cold-rolled Ti-24Nb-4Zr-8Sn alloy. (g) HAADF-STEM image showing the nanoscale hexagonal ω phase layer formed at {112} deformation twin boundary, marked by red and green color dashed lines; (h) HAADF-STEM images showing the unit cell of hexagonal ω phase and BCC β phase.(i) is the distribution of thicknesses of ω phase at twin boundaries in different VEC cases from published papers. [44–46, 54, 78–80]. The solid points in the middle of the lines indicate the value of average thickness of local ω phases at the twin boundaries weighting by the length. Error bar is based on the weighted standard deviation of the data points

and thermomechanical processing procedures, which are not in the scope of this paper but will be explored in the future. Besides, as indicated by the error bar magnitudes, the fluctuations of ω phase thicknesses also decrease as VEC increases, which means that twin boundaries are rough in low VEC cases due to the fluctuations of many local ω phases on the boundaries, while they become flat as VEC increases. This trend is also consistent with observations in our MD simulations in Figures 6 and 7 (d)-(f).

Above all, the experimental observations of the morphology of ω phases at the twin boundaries and the VEC effect on ω phases formation behavior at twin boundaries are generally consistent with the observations in DFT and MD simulation results. However, it should be emphasized that the above analyses are based on the results of electron microscopy characterizations from different sources. The accuracy of these results depends on the quality of characterizations and the sampling of different locations in alloy samples. These factors are difficult to control. Thus, the results in Figure 7(i) can only be used as supportive evidence of our conclusions about {112} twin boundary structures in β-Ti alloys.

3.3 Growth of {112} twin embryos

So far, our DFT calculations and MD simulations reveal the correlation between the stability of {112} twin embryos and $\beta \rightarrow \omega$ phase transformation at {112} twin boundaries. In the next step, we deformed the twinned supercells by applying the shear loading to examine the growth kinetics of the stable twin embryo with the minimum {112}-layer thickness for each composition identified from Figure 6 (3 layers for pure Nb, 6 layers for TiNb and Ti_2Nb, and 9 layers for Ti_3Nb). Thus, after the MD relaxations in Section 3.2, we deformed the supercells with the stable twin embryos using a constant engineering shear strain rate along [111] direction on $(11\bar{2})$ plane at 300 K. The corresponding shear stress-strain curves are plotted in Figure 8. As shown in Figure 8 (b), (c), and (d), the twin embryos in pure Nb, TiNb, and Ti_2Nb can smoothly grow under the applied shear loading. From the inserted snapshots in the plots of Figure 8 (b)-(d), the twin regions all become much thicker than the initial twin embryos when the shear strain increases to 0.20. Another interesting finding is that the shear stress needed for twin boundary migration in pure Nb is around 0.7 GPa, which is much larger than the other two alloys (Ti_2Nb and TiNb). The increase in the critical stress for twin migration is likely related to the high twin boundary energy of pure Nb (278.7 mJ/m^2 from our calculation) compared with those of Ti_2Nb and TiNb shown in Figure 4.

In addition, the stress-strain curve in pure Nb in Figure 8 (d) behaves like periodic peaks and each peak has almost the same maximum stress. It suggests the twin migration in pure Nb is triggered by just one type of mechanism with the same critical stress, such as the twin boundary step nucleation. However, the stress-strain curves for Ti_2Nb and TiNb in Figure 8 (b) and (c) have more fluctuations on the maximum value of each local peak, especially for Ti_2Nb where there are still some ω phases on twin boundaries as shown in Figure 7 (e). Since each peak of the stress-strain curve corresponds to the critical stress to trigger the twin boundary migration, these fluctuations suggest the variations of local chemical concentrations may change the detailed mechanism of the rate-limiting step of twin migration. Since there are stronger fluctuations in the stress-strain curve of Ti_2Nb (Figure 8 (b)) than those for TiNb (Figure 8 (c)), ω phases on twin boundaries of Ti_2Nb could affect the critical stress

that triggers the rate-limiting step of twin migration by considering that there are much more ω phase or ω-like structures on twin boundaries of Ti_2Nb (Figure 7 (e)) than those on twin boundaries of TiNb (Figure 7 (f)). In Supplementary Materials, we also provide twin embryo growth movies for Ti_3Nb (Supplementary Movie 1), Ti_2Nb (Supplementary Movie 2), and pure Nb (Supplementary Movie 3). The effects of ω phases on twin boundary migration and twin embryo growth kinetics will be further discussed in the following sections.

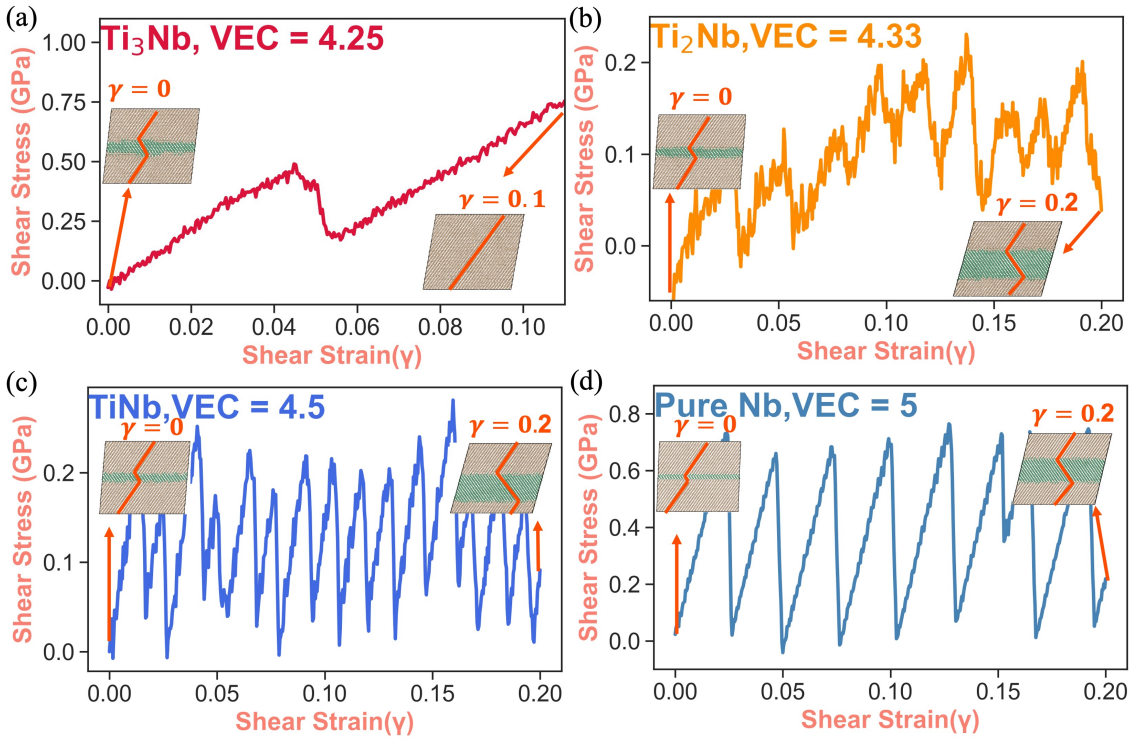

Figure 8: Stress-strain curves and atomistic structure changes when constant shear loading is applied to supercells that contain stable twin embryos with the minimum {112}-layer thickness for different Ti alloys. Inserted graphs in each subfigure are the snapshots at the initial state and the final state of the shear process. (a) Ti_3Nb starting from a relaxed 9-layer twin embryo. (b) Ti_2Nb starting from a relaxed 6-layer twin embryo. (c) TiNb starting from a relaxed 6-layer twin embryo. (d) Pure Nb starting from a relaxed 3-layer twin embryo. Atoms marked in light brown color in the inserted figures are in the BCC matrix while atoms marked in green color in the inserted figures are in the BCC twin. The orange solid lines in the inserted figures indicate the crystal orientations of the BCC phase.

In contrast, the stress-strain curve and the corresponding twin embryo evolution for Ti_3Nb shown in Figure 8 (a) are abnormal compared with all other alloys in Figure 8. Even though a 9-layer twin can survive after a long-time MD relaxation at room temperature, its twin boundaries do not move and the twin embryo does not grow as the shearing strain increases from zero. This low twin boundary mobility could be related to the high ratio of ω phases on twin boundaries shown in Figure 7 (a) and (d), which could significantly increase the roughness of twin boundary energy landscape and the energy barriers for twin boundary migration. When the shear strain is above ~0.03, a slope change of the stress-strain curve occurs due to some internal structural variations, which are found

to be diffusionless phase transformation inside the twin embryo as analyzed in the following section. This twin embryo even starts to shrink when the shear strain increases above 0.0448 and completely disappears when the shear strain reaches ~ 0.06. Then the shear stress continues to increase with the shear strain without further twinning behavior. When the shear strain approaches 0.1, we can only see a single crystal without a twin embryo according to the right inserted graph in Figure 8 (a).

Figure 9 demonstrates the detailed evolution of atomistic structures during the shrinkage of the twin embryo for Ti_3Nb shown in Figure 8 (a). As shown in Figure 9 (a), we present several snapshots of the twin region at/near some critical points of this detwinning process. We can observe α'/α" phases (purple color atoms) accumulate in the twin region and then disappear during the detwinning process. Here, we use the PTM method to identify different phases, but the PTM method cannot distinguish the difference between α' (HCP) and α" (orthorhombic) phases due to their similar atomistic structures (PTM simply identifies α' and α" phase as HCP phase). In the following sections, to more rigorously elaborate and avoid any misunderstanding, we use the α'/α" phase to represent the PTM-identified HCP phase. We also provide a total number of atoms in α'/α" phases for each time step in Supplementary Movie 1. In this movie, the number of atoms in α'/α" phases continuously increases and approaches a maximum value when the time step is 112000 (corresponding shear strain γ is 0.0448.). This indicates BCC twin $\rightarrow$ α'/α" phase requires the accumulation of enough stress inside the twin embryo. When shear strain further increases, based on the stress-strain curve in Figure 8 (a) and the snapshots in Figure 9 (a), the sudden stress drop together with the detwinning behavior should be related to the α'/α" phase $\rightarrow$ BCC matrix within the twin embryo. Meanwhile, we can observe low mobility of twin boundary (specifically lower twin boundary) both in Supplementary Movie 1 and Figure 9 (a) during the detwinning process, which is for the sake of pinning effect from ω phase at the twin boundary. In Supplementary Movie 4, we also show the video of the detwinning process from the top view (along $[\overline{1}\overline{1}2]_\beta$ direction normal to the twin plane).

To more thoroughly analyze the phase transformation behaviors during the detwinning process in the twin region, we compare the structures of twin regions at some critical states of detwinning process, as shown in Figure 9 (a). Red dashed lines mark the initial locations of twin boundaries before shear is applied. When shear strain γ is 0.0384, there are some small local α'/α" phases mainly distributed at the upper twin boundary and the volume of the twin region has a tendency to decrease compared to the initial state (γ equals to 0). As the shear strain γ increases to 0.05, the twin region further shrinks. Compared to the structure of the twin region when γ is 0.0384, the initial α'/α" phases (purple color) have transformed to BCC matrix (light brown) and more atoms in the middle part of twin region (green color) becomes α'/α" phases. Further, when shear strain γ slightly increases to 0.056, the twin region disappears and totally transforms into BCC matrix, and the intermediate α'/α" phases no longer survive. Based on this boundary to interior detwinning process within the twin region, we propose an α'/α"phases-assisted detwinning mechanism, and we illustrate the step-by-step process in Figure 9(b)-(f).

As shown in Figure 9 (b), to illustrate the detwinning process in Ti_3Nb more clearly, we start from the perfect single crystal. Here we assign the label index for each atomic layer along $[11\bar{2}]$ direction, ranging from -9 to 14 shown on the left side of Figure 9(b). Then we construct a 4-layer twin embryo in the middle of the supercell following the layer-by-layer twin dislocation slip mechanism, as shown

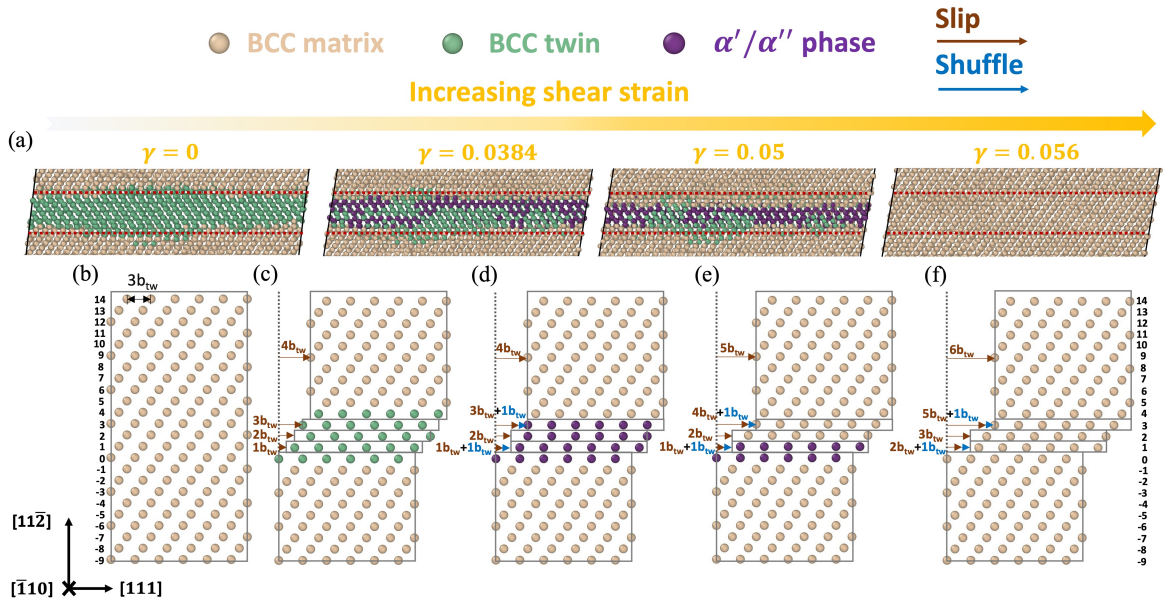

Figure 9: Evolution of atomistic structures during the shrinkage of the twin embryo in Ti_3Nb under the increasing shear strain along the twinning direction. (a) shows the snapshots of the twin region (green color) at/near some critical points of this detwinning process during the MD simulations. (b)-(f) are schematic illustrations for the whole process of the initial twinning from a perfect single crystal and the later detwinning process in Ti_3Nb assisted by reversible β (BCC twin variant) to α'/α" phase to β (BCC matrix variant) phase transformation. Here BCC matrix is in light brown color, α'/α" phase is in purple color, and BCC twin is in green color. During the twinning and detwinning process, atomic displacements by slip are marked in dark brown arrows, while atomic displacements by shuffle are marked in blue arrows. The magnitudes of atomic displacements shown in (c)-(f) are calculated in reference to the initial state of the perfect crystal in (b). The label index of each atomic layer along [11$\bar{2}$] direction is shown on the left side of (b) and the right side of (f). Here one twin Burgers vector $b_{\mathrm{tw}} = \frac{1}{6}[111]$.

in Figure 9 (c). Even though {112} twin nucleation in Ti_3Nb and other metastable β-Ti alloys may not follow this slip mechanism, the net relative fault displacements in the twinned region compared to the initial perfect crystal state should be independent of the specific twin formation pathways. At the stage in Figure 9 (c), when the twin embryo is hard to grow even under external shear along the twinning direction (possibly due to the pinning effect of ω phase at the twin boundaries), α'/α" phase-assisted detwinning behavior happens inside the twin region. As shown in Figure 9 (d), by shuffling Layer 1 and Layer 3 along [111] direction in the magnitude of one twin Burgers vector ($b_{\mathrm{tw}} = \frac{1}{6}[111]$), four atomic layers of the distorted α'/α" phase form (purple atoms). This stage corresponds to the stage when γ is 0.0384 in Figure 9 (a). Further, Layer 3 to Layer 14 undergo a rigid slip in the magnitude of 1 b_{tw}, approaching the stage shown in Figure 9 (e). Compared to Figure 9 (d), the upper twin region (Layer 2 and Layer 4) has transformed back to BCC matrix from the intermediate α'/α" phase, which is similar to the stage when γ is 0.05 in Figure 9 (a). Similarly, from Figure 9 (e) to Figure 9 (f), the lower part of α'/α" phase totally transforms into the BCC matrix by slipping Layer 1 to Layer 14 for 1 b_{tw}, and finally all twin region disappears as shown in Figure 9 (f). In total, compared to the original perfect structure (Figure 9 (b)), atoms in Layer 1 and Layer 2 have a total displacement of 3 b_{tw} (equivalent to one full Burgers vector), while atoms in Layer 3 and above part are displaced by 6 b_{tw} (equivalent to two full Burgers vectors). The magnitudes of net displacements are also consistent with our MD results by analyzing the average atomic displacements.

Here, for simplicity, we use a 4-layer twin embryo structure for illustration. Moreover, the smallest thickness to identify α'/α" phase along $[\bar{1}10]_{\beta}$ || $[010]_{\alpha''}$ || $[000\bar{1}]_{\alpha'}$ direction is a length of 4 atomic layers as shown in Figure 1 (a). Indeed, the whole detwinning process presented in Figure 9 (c)-(f) can be assumed as the detwinning process of the upper twin region of 9-layer twinned supercell in Ti_3Nb. In general, the detwinning process for a stable twin embryo in metastable β Ti alloys can happen by repeating the steps from stage in Figure 9 (d) to stage in Figure 9 (f), starting from a twin boundary to the interior of the twin region.

Even though the detwinning behavior can happen with the assistance of α'/α" phase, it needs the premise of low mobility of the twin boundaries even under loading conditions. In other words, twin boundaries in Ti_3Nb are relatively hard to move along the twinning direction. Meanwhile, the extra displacements within the twin region induced by shuffle illustrated in Figure 9 (d) and (e) have the anti-twinning sense, which indicates that twinning in BCC matrix region and anti-twinning in BCC twin region become competitive in metastable β Ti alloys. Direct investigation of twinning and anti-twinning behaviors in metastable β Ti alloys under loading conditions is difficult, but we can indirectly compare the twinning and anti-twinning preference by investigating the energy barriers of twin growth fault generation at twin boundaries by applying homogeneous displacements as described in Section 2.5. The corresponding results and detailed discussion are shown in the following part.

Figure 10 shows the results of energy barriers and stability of 2-layer twin growth faults vs the magnitude of the homogeneous displacements for pure Nb and different Ti-Nb alloys. Detailed illustrations for the twin growth faults generation and twin growth fault energy calculation are explained in Section 2.5. Figure 10 (a) shows the structure snapshots at some critical points during the 2-layer twin growth faults generation process in pure Nb. Green color represents BCC twin and light brown color represents BCC matrix. The orientations of the BCC twin and BCC matrix are consistent

with those defined in Figure 3. White atoms, which are identified as the "Other" phase by the CNA method in OVITO [69–71], are at the twin boundary or in the twin growth faults. Snapshot A is the initial structure before twin growth faults generation. Snapshot B, C, and D are atomistic structures at the transition state of the first energy barrier, the local energy minimum, and the transition state of the second energy barrier in the twin growth fault energy profile, respectively. Snapshot E is the structure containing 2-layer twin growth faults with one full Burgers vector displacement fault magnitude. From the crystallography view, Structure A and structure E should be the same for pure metals and the energy states should also be similar for alloys as long as the area of stacking planes defined by the supercell is large enough.

Figure 10 (b) is the energy profile of 2-layer twin growth faults by homogeneous displacements as described in Figure 3 along the twinning directions for Ti-Nb alloys and pure Nb. Theoretically, based on the classical layer-by-layer twin dislocation slip mechanism, there is a local energy minimum when λ is $\frac{1}{3}$ (equivalent to the magnitude of one twin Burgers vector b_{tw}), indicating twin growth by one {112} atomic layer (From stage A to stage C). However, because of an isosceles feature of {112} twin boundaries [40,72,81,82], the positions of local energy minimum may vary. If we continue to increase the magnitude of fault displacements along the twinning direction after the local energy minimum, the twin growth fault structure first increases and then decreases to approach stage E, so the structure evolution through C to E can be regarded as the detwinning behavior of the twin region through slip along the twinning direction. Meanwhile, since stage E is structurally equivalent to stage A, twin growth can be achieved either by shearing one twin Burgers vector along the twinning direction (from stage A to stage C) or two twin Burgers vectors along the opposite direction (anti-twinning direction) (from stage E to stage C). In pure Nb and other BCC transition metals, the energy barrier for twin growth along the anti-twinning direction (from stage E to stage C), which is close to the energy barrier for detwinning behavior (from stage C to stage E), is much larger than the energy barrier along the twinning direction (from stage A to stage C) [72]. This indicates that in most BCC transition metals, {112} twins prefer to grow by shearing along the twinning direction, and the anti-twinning or detwinning phenomenon is hard to observe under loading conditions.

As we compare the energy profiles of 2-layer twin growth faults in Ti_3Nb with pure Nb and other Ti-Nb alloys shown in Figure 10 (b), it is evident that the difference of the energy barrier for anti-twinning (marked by star symbols) and the energy barrier for twinning (marked by hexagon symbols) greatly reduces. The ratio of the energy barriers for anti-twinning ($\gamma_{\mathrm{TGF}}^{\mathrm{AT}}$) and twinning ($\gamma_{\mathrm{TGF}}^{\mathrm{TW}}$) is around 17 in pure Nb, and the values of $\gamma_{\mathrm{TGF}}^{\mathrm{AT}}/\gamma_{\mathrm{TGF}}^{\mathrm{TW}}$ decrease as the VEC of the alloys decreases: 8.5 for TiNb, 3.4 for Ti_2Nb and 1.48 for Ti_3Nb. Clearly, the small difference of energy barriers for twinning and anti-twinning in Ti_3Nb alloy means that twin growth behavior in the BCC matrix and anti-twinning in BCC twin (alternately speaking, detwinning behaviors) are competitive given the applied shear strain along the twinning direction, making the detwinning behavior through the anti-twinning mechanism through C to E in Figure 10(a) much more likely to occur. In summary, the energy profile for 2-layer twin growth faults can indicate the intrinsic energetic preference of twinning behavior in the BCC matrix and anti-twinning behavior in the BCC twin (or detwinning behavior). When energy barriers are comparable, and intermediate α'/α" phases in Figure 9 can further promote the detwinning event and so the twin embryos do not grow even though applying shear along twinning

directions.

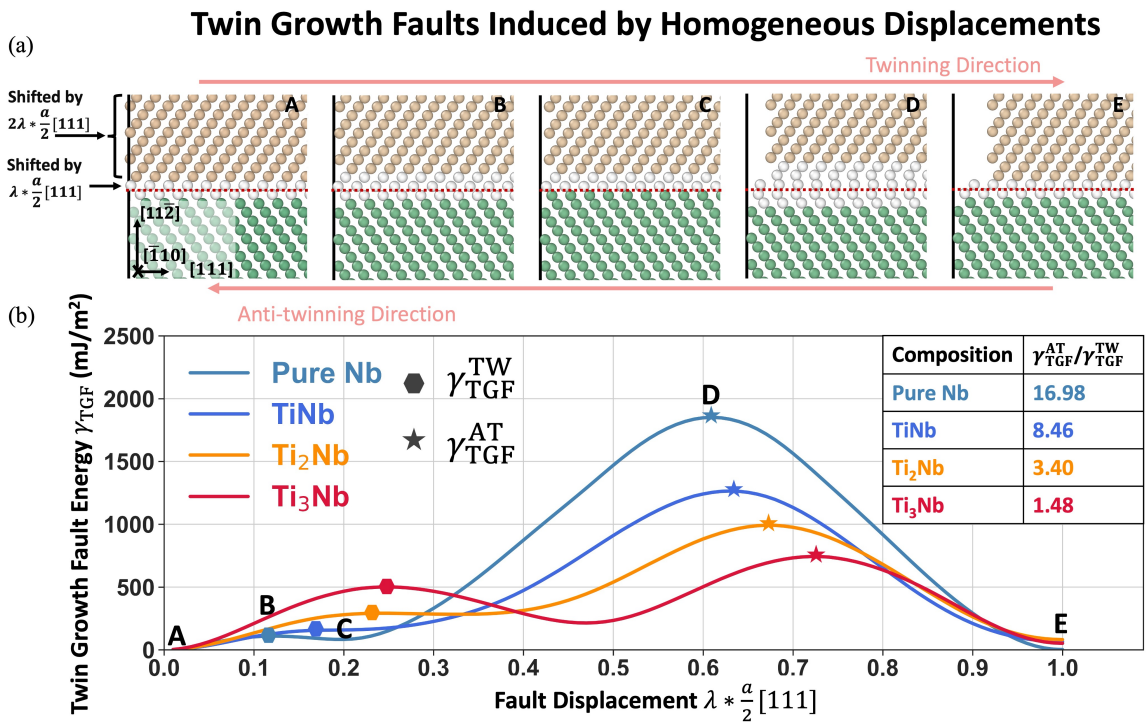

Figure 10: The energy profiles of 2-layer twin growth faults induced by $\lambda \times \frac{1}{2}[111]$ homogeneous displacements (described by Section 2.5) in Ti-Nb alloys and pure Nb. (a) shows the structure snapshots at some critical stages during the 2-layer stacking twin growth faults generation process in pure Nb. The colors of atoms and the red dashed line have the same meaning as those defined in Figure 3. Stage A is the initial state before twin growth faults generation (λ=0). Stage B, C, and D are at the transition state of the first energy barrier, the local energy minimum, and the transition state of the second energy barrier of the twin growth fault energy profile, respectively. Stage E is the state when the displacement fault magnitude equals one full Burgers vector (λ=1). (b) shows the plots of the energy profile of 2-layer twin growth faults for different Ti-Nb alloys and pure Nb as a function of $\lambda \times \frac{1}{2}[111]$ displacements. The star symbols in the plots mark the stage D location of energy barriers for anti-twinning (γ_{TGF}^{AT}), while the hexagon symbols indicate the stage B location of energy barriers for twinning (γ_{TGF}^{TW}). The inserted table shows the value of $\gamma_{TGF}^{AT}/\gamma_{TGF}^{TW}$ in metal/alloys with different compositions.

Based on the detwinning phenomena for Ti_3Nb described above, two different reversible phase transformations occur: $\beta \leftrightarrow \omega$ transformations at twin boundaries and $\beta \leftrightarrow \alpha$'/$\alpha$" transformations inside twin embryos. A large amount of $\beta \rightarrow \omega$ transformations on {112} twin boundaries for Ti_3Nb reduce the twin mobility and increase the stress level that can be reached inside the twin embryos. Such high stress and relative low β phase stability for Ti_3Nb at 300 K together induce the β twin $\rightarrow$ α'/α" $\rightarrow$ β matrix transformations inside twin embryos. In addition, the close distances between two {112} twin boundaries in this 9-layer twin embryo also play a role in activating the final detwinning behavior. We also constructed an 18-layer twinned supercell for Ti_3Nb and performed the same shear loading. The twin embryo does not smoothly grow as well (only locally grow/shrink) under the applied stress, confirming $\beta \rightarrow \omega$ transformations on {112} twin boundaries for Ti_3Nb reduce the twin mobility independent of the twin embryo size. Meanwhile, α'/α" -phase-like structures frequently

form locally but they would not continue to grow to bulk α'/α" phase and disappear shortly. In all, the 18-layer twin growth behavior compared to the 9-layer twin detwinning behavior indicates that total detwinning is conditional and requires a narrow twin embryo in these MD simulations with high strain rates.

3.4 Controlling {112} twin growth by tuning β phase stability

By analyzing the MD results thus far, we have investigated how different phase transformations affect the {112} twin embryo growth. The next question is whether we can control the growth of {112} twin by tuning the thermodynamics of phase transformations. Reversible phase transformations are highly related to relative phase stability, which can be tuned by both temperature and alloy compositions. Therefore, we investigate how temperature and alloy compositions affect the detwinning/twinning phenomena of a 9-layer twin embryo in alloys with compositions similar to Ti_3Nb.

The detailed results are in Figure 11 (all compositions in Figure 11 are in the atomic fraction). As for the temperature factor for a Ti-Nb alloy with fixed 25% Nb composition, by comparing the shear stress-strain curves of Figure 11 (a)-(d), we find that the detwinning behavior is suppressed and the twin embryo can smoothly grow when the temperature increase to 400K. Based on the fitting results of interatomic potential [66] we use in our study, β phase is thermodynamically stable in Ti_3Nb when temperature greater than 410 K. Meanwhile, we find that when the temperature approaches 400 K, there are fewer ω structures along twin boundaries compared to those in 300 K. The increase of BCC phase stability can suppress the formation of the local ω phase inside twin boundaries. Without too many local ω-like structures forming along the twin boundaries, though we can still observe stress-induced α'/α" nuclei frequently form within the twin embryo, α'/α" phase nuclei are hard to grow. This is because the local stress within the twin embryo is hard to accumulate but would be released by fast {112} twin boundary migration.

Moreover, we also investigate how compositions affect detwinning behavior at a constant temperature (e.g., 300 K). Based on the fitting results of Ti-Nb MEAM potential [66], Ti_3Nb is very close to the critical composition where ω phase is relatively unstable compared to β phase at 0 K. Hence, we gradually increase the Nb concentration and observe the stress-strain curves and the corresponding twin embryo evolution kinetics at 300 K. When Nb concentration equals 26 % in Figure 11 (e), an interesting partial detwinning behavior occurs, with the snapshots of the supercells at different shear strains viewed from the twin Burgers vector direction [111] in Figure 11 (i)-(l). As we can see from Figure 11 (j) and (e), when shear strain approaches 0.05, the stress drops and the partial twin embryo becomes the α'/α" phase. Thereafter, the twin boundary has a tendency to migrate locally (green color outside the red rectangle that defines the initial twin embryo region in Figure 11(i)). The reduced stress when the strain is larger than 0.05 is achieved by both for local BCC twin $\rightarrow$ α'/α" phase transformation and local twin migration. With the further increase of shear strain to 0.114 (Figure 11 (e)), the partial detwinning occurs since the local α'/α" phase Figure 11 (i) totally transforms into a BCC matrix as plotted in Figure 11 (k). Then the twin boundaries of the surviving twin embryo migrate slowly. Compared to Ti_3Nb, twin boundaries in $Ti_{0.74}Nb_{0.26}$ have a slightly higher twin mobility. Hence, local stress within the twin embryo can be partially released when twin boundaries migrate locally. At this stage, the local stress concentration can not be satisfied for a

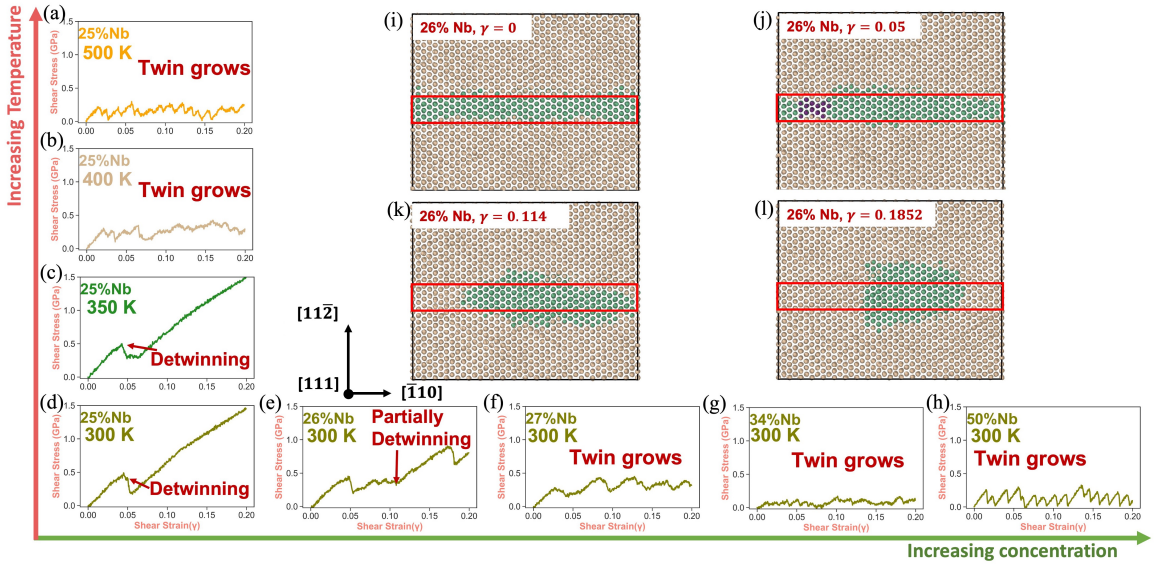

Figure 11: Shear stress-strain curves for 9-layer twin embryo for different compositions under different temperatures. (a)-(d) are all for Ti_3Nb but at different temperatures. (d)-(h) are all at 300K but at different compositions. (i)-(l) are the snapshots for $Ti_{0.74}Nb_{0.26}$ during deformation viewed from the shear direction [111]. The red rectangle in the (i)-(l) represents the twin boundary of the stable twin embryo before applying the shear loading. Light brown color in (i)-(l) represents BCC matrix, purple color represents α'/α" phase, and green color is for BCC twin. The phase identification is completed by Polyhedral template matching (PTM) [67]and Grain segmentation method [68].

complete BCC twin $\rightarrow$ α'/α" phase $\rightarrow$ BCC matrix phase transformation.

As shown in Figure 11 (d)-(g), when the Nb concentration approaches 27 % and above, the twin can smoothly migrate under the applied shear stress. It is worth noticing that the critical stress for twin migration has a tendency to drop as Nb concentration increases initially by comparing the case with 27 % Nb in Figure 11 (f) ($\sim$ 0.4 GPa for twin migrations) to the case with 34 % Nb in Figure 11 (g) ($\sim$ 0.1 GPa for twin migrations). Then the critical stress for twin migration increases when the Nb concentration further increases as shown in the case with Nb concentration equal to 0.5 in Figure 11 (h) ($\sim$ 0.3 GPa for twin migrations). This trend would be further kept with the increasing Nb concentration since the critical stress for twin migration in pure Nb in Figure 8(d) reaches $\sim$ 0.7 GPa. (In Section S6 of Supplementary Materials, we provide stress-strain curves of more compositions in the region of Nb atomic concentrations from 27% to 50% (VEC value of the Ti-Nb alloy increases from 4.27 to 4.5, correspondingly). Since the increases of Nb concentrations can reduce the stability and amount of ω phases on twin boundaries as shown in Figures 5- 7, these variations of Nb effects suggest that there could be multiple factors that determine the roles of ω phases on {112} twin migration kinetics, which will be discussed in the next section.

4 Discussions

In this study, we shed light on the role of ω phase in the {112} twin growth in β-Ti alloys, and the results uncover the fact that it may highly depend on the ω phase stability compared to the β phase. Many previous studies have observed that {112} twins in β-Ti alloys have close relationships with structural phase transformation between ω and β phase [14, 44–54]. Nevertheless, there is a long debate on whether ω phase can promote or impede {112} twin growth. In this study, shear stress-strain curves shown in Figures 8 and 11 combined with twin boundary configurations shown in Figure 7 (d)-(f) indicate that both promotion and impediment behaviors of ω phase can happen under different conditions as described in Section 3.4. These opposite effects indicate that the kinetics of {112} twins in β-Ti alloys may be related to complex mechanisms of diffusional phase transformations between ω and β phase that are decided by multiple factors and parameters.

A schematic illustration of the possible mechanism to explain the above concentration-dependent ω phase effects is shown by the free energy landscape for the homogeneous diffusionless β matrix $\rightarrow$ ω phase $\rightarrow$ β twin transformations in Figure 12. In this plot, as the VEC decreases from Figure 12 (a) to (c), ω phase becomes more stable, so the free energy of ω phase at its ground state goes down, and it is reasonable to assume that the local curvature of the free energy curve (the reciprocal of the local curvature radius) at its ground state may also increase because the energy cost to break its ground-state symmetry structure generally arises with its enhanced stability; meanwhile, under the same trend of VEC changes from Figure 12 (a) to (c), the free energy of β phase at its ground state goes up relative to that of ω phase, and the local curvature of the free energy curve may also decrease at the ground state of β phase because the energy cost to break its ground-state symmetry structure generally drops with its weakened stability. Because of the existence of ω phases on the {112} twin boundaries in many β-Ti alloys, we can assume the free energy landscape of the homogeneous diffusionless transformation of β matrix $\rightarrow$ ω phase $\rightarrow$ β twin is strongly correlated to the kinetics of {112} twin boundary migration, so a low/high energy barrier along the free energy landscape of this homogeneous transformation can correspond to the fast migration kinetics. As shown in Figure 12, there is an energy barrier of ΔG_a from the ground state of β matrix to the ground state of ω phase, and there is another energy barrier ΔG_b from the ground state of ω phase to the ground state of β twin. Thus, the overall twin migration kinetics could be related to the larger value of ΔG_a and ΔG_b in this whole transformation path from β matrix to β twin.

Due to the changes in the positions and shapes (local curvatures near the ground states) of free energy curves of both β and ω phases illustrated in Figure 12, we can see the variations of the larger value of ΔG_a and ΔG_b can be used to explain the role of ω phase on the {112} twin growth kinetics. When VEC is large ($\sim$ 4.5 at 300 K), ΔG_a is much larger than ΔG_b (Figure 12 (a)), indicating there could be large barriers to achieve the transformation path from β matrix to β twin through ω phase as the intermediate phase, and the twin migration can be achieved by other mechanisms (such as the twin dislocation mechanisms [40]). When VEC decreases ($\sim$4.33 at 300 K), ΔG_a decreases and ΔG_b is also relatively not large (Figure 12 (b)), indicating ω phase as the intermediate phase can provide a low-barrier transformation path from β matrix to β twin. When VEC further decreases ($\sim$ 4.25 at 300 K), both ΔG_a and ΔG_b can increase again compared with those in Figure 12 (b), indicating the twin migration kinetics is slowed down again. Meanwhile, as ω phase become stable at low VEC

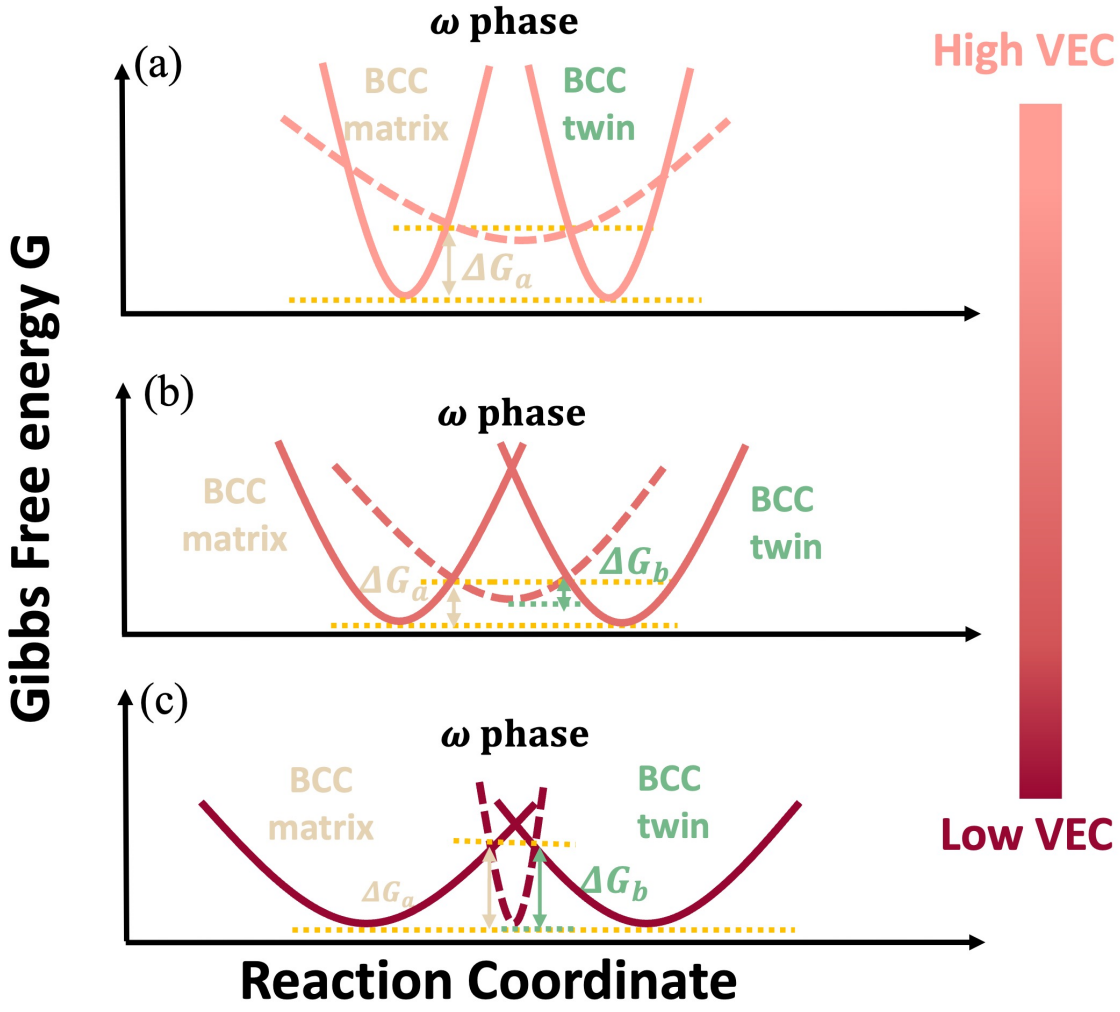

Figure 12: Schematic draw of the free energy landscape variations for the homogeneous diffusionless transformations to indicate the variation of twin boundary migration kinetics. In each subfigure, solid curves represent the BCC matrix and BCC twin (left and right), respectively; the dashed curve in the middle is for the ω phase. The color bar for the free energy landscape curves is shown on the right of the figure. Darker red is for lower VEC Ti alloys while lighter red is for higher VEC Ti alloys. ΔG_a in the plots represents the energy barrier of BCC matrix $\rightarrow$ ω phase transformation and ΔG_b represents the energy barrier of ω phase $\rightarrow$ BCC twin transformation. Since ΔG_b in (a) is very small, we do not mark it there.

conditions, they can locally form in different orientations and can grow or shrink in different directions under loading conditions, which further complicates the {112} twinning pathways. Here we have to emphasize that the plots of free energy landscape are used for illustration purposes only. They should not only be governed by VEC but also other factors, such as chemical composition variations beyond the d-band filling effects, temperature, applied stress, etc. An accurate free energy landscape of metastable phases in Ti alloys will be investigated in future work to provide quantitative guidance on manipulations of twin activities based on thermodynamic phase stability. In addition, the quantitative correlation between the free energy landscape in the homogeneous diffusionless transformation and the twin migration kinetics through heterogeneous mechanisms (e.g., twin boundary step formation and migration) should also be studied in detail. A possible strategy is to investigate how the free energy landscape in the homogeneous diffusionless transformation affects the energy profiles of twin growth faults in Figure 10, which can be regarded as simplified mechanisms of the realistic twin boundary migration kinetics. The free energy landscape of reversible phase transformations can be accurately explored for complex alloy compositions based on atomistic simulations and CALPHAD (CALculation of PHAse Diagrams) methods, and twin growth fault energy profiles can also be calculated by atomistic simulations with accurate interatomic potentials or direct first-principles calculations.

Though our results illustrate that the stability and growth kinetics of the pre-existing {112} twin embryos are highly related to the diffusionless transformation between metastable phases in β Ti alloys, we did not investigate the correlation between phase transformation and {112} twin nucleation in this study. In experiments, {112} twin nuclei were observed inside the ω nano-particles in β Ti alloys, so it was proposed that {112} twins were nucleated from the ω phase [46], but the real dynamics of twin nucleation is difficult to be captured experimentally. In this work, we do not intend to extensively investigate the relationship of phase transformations and {112} twins nucleation in various types of Ti alloys. Instead, we apply MD simulations to demonstrate that {112} twins in Ti_3Nb prefer to nucleation from grain boundaries instead of local ω clusters or particles. Specifically, we compare the twin nucleation behaviors in Ti_3Nb alloy under three different conditions: 1) shearing along the twinning direction for a perfect single crystal, 2) shearing along the anti-twinning direction for a perfect single crystal, and 3) shearing a bicrystal containing twist grain boundaries [83]. The detailed description of twist grain boundary construction is in Supplementary Section S7.1. According to the stress-strain curves shown in Supplementary Section S7.2, {112} twins can nucleate either by shearing along twinning or anti-twinning directions with a comparable critical shear stress, which is consistent with the results of $\gamma^{\mathrm{AT}}_{\mathrm{TGF}}/\gamma^{\mathrm{TW}}_{\mathrm{TGF}}$ for Ti_3Nb in Figure 10 (c). In addition, compared to the twin nucleation behaviors in single crystals, twins can nucleate more easily under relatively smaller shear stress and much smaller shear strain from grain boundaries in the bicrystal case. In Supplementary Section S7.3, we also present the snapshots of the whole process of twin nucleation and evolution. The results show twins directly nucleate from the grain boundaries and then annihilate under the increased strain, consistent with the detwinning behavior of the twin embryo in Ti_3Nb plotted in Figure 8(a) and Figure 9 (a). Meanwhile, we do not observe a significant amount of local ω phases before twin nucleation in all three cases, but we can observe thick ω phases form around the twin boundaries from the cross-section views after twin nucleation. The formed thick ω phases do not promote the twin growth and totally disappear once the twin totally shrinks. These MD simulations suggest that, at

least for Ti alloys with VEC values $\sim$ 4.25 or higher at 300 K, the local ω phases are more likely to be products of {112} twins formed from grain boundaries and other defects, which are preferred twin nucleation sites compared with local ω phases. However, for Ti alloys with even lower VEC values and a large amount of athermal ω phases, {112} twin nucleation promoted by ω phases could be possible.

Besides effects of ω phase and defects like grain boundaries on {112} twinnability, oxygen is also an important factor controlling the {112} twinnability, which is not mentioned in this study. In experiments, oxygen is highly soluble in Ti alloys and solubility of oxygen is inevitable during mechanical processing [3]. Meanwhile, it is widely acknowledged that oxygen content plays important roles in deformation mechanisms and phases stability in β-Ti alloys [84–89], especially ω phase stability, α'/α" phase stability, and phase transformation between multiple metastable phases [84,86,87,90–92]. Generally, it is widely observed that high-level oxygen content can suppress the formation of ω phase [86,90] and increase the stability of β phase in the β-Ti alloys [84,87]. Hence, oxygen can also affect the free energy landscape of ω phase and β phase and so further control the {112} twin growth. Meanwhile, the solubility of oxygen can reduce the volume fraction of stress-induced α'/α" phase in β phase and so increase the difficulty of β phase $\rightarrow$ α'/α" phase transformation [87,93]. Therefore, it is necessary to include oxygen effects in the future twinnability investigation in Ti alloys.

Our MD results reveal the α'/α" phase-assisted detwinning of {112} twin (Figure 9). However, this detwinning behavior may be hard to be observed in experiments. As illustrated in the above discussion, one possible reason is that the solubility of oxygen in real experiments can suppress the β phase $\leftrightarrow$ α'/α" phase and so α'/α" phase may not serve as the intermediate state for reversible β phase transformations in {112} twins as explained in Figure 9 (b). Other possible reasons are that the shear strain rates in MD simulations are much larger than those in experiments and microstructures of alloy in real experiments contain complex defects that change the free energy landscape of twin nucleation and growth. As illustrated in Section 3.4, detwinning behavior is decided by competition between BCC phase $\leftrightarrow$ α'/α" phase inside twin embryo and BCC phase $\leftrightarrow$ ω phase along twin boundaries. So detwinning behavior happens at the condition of low twin mobility of twin boundaries and large stress accumulating inside the twin embryo in a short time. In experiments, the samples contain various types of defects to release external stress and/or trigger the twin migration under much lower shear strain rates compared with MD simulations. Moreover, twin propagation and growth are generally in the intersonic speed [94] and in-situ techniques are hard to capture the intermediate phase for twinning and detwinning. Despite these inconsistent conditions for the {112} twin embryo growth kinetics between atomistic simulations and experiments, our MD simulations indeed confirm that {112} twin embryo growth can become much more difficult when the VEC is below a critical value ($\sim$ 4.25 at 300 K).

5 Conclusions

In summary, we conduct DFT calculations and classical MD simulations to investigate the {112} twin embryo stability and growth behaviors in β-Ti alloys comprehensively by varying twin embryo sizes, alloy compositions, and temperatures. Our findings are listed below:

1) Dependent on alloy compositions and the related VEC values, {112} twin boundary structures

would activate the local β to ω phase transformations along the twin boundaries. As the VEC value decreases, ω phases on twin boundaries become thicker and increase the roughness of twin boundary planes. These tendencies are generally in agreement with experimental characterizations of {112} twin boundary structures in different β-Ti alloys from this study and literature [44–46, 54, 78–80]. Consistent with tendencies, both DFT results at 0 K and MD results at 300 K reveal that stable stacked ω structures would destabilize the twin embryo in low VEC cases (equal or less than 4.25 in this study), so the twin embryo should be much thicker (at least 9 atomic layers of {112} twin planes) for survival than those β-Ti alloys with high VEC values (6 or 3 atomic layers of {112} twin planes when VEC equal or greater than 4.5). This stability requirement for twin embryos can significantly reduce the {112} twin nucleation kinetics/rates in certain β-Ti alloys, where both β phase and ω phase have similar thermodynamic stability.

2) Besides twin embryo nucleation, β to ω phase transformations in β-Ti alloys can also affect the {112} twin growth under the applied shear stress and the effects vary with alloy compositions. In low VEC cases (equal or less than 4.25 at 300K in this study), ω phase transferred from metastable β phase at twin boundaries can greatly impede the twin migration; meanwhile, BCC twin $\rightarrow$ α'/α" phase $\rightarrow$ BCC matrix phase transformations can also be triggered within the {112} twin embryos by the external shear stress and result in twin embryo eliminations. The occurrence of this α'/α" phase-mediated detwinning behavior may benefit from a small difference between the energy barrier of the twinning behavior in BCC matrix and the energy barrier of the anti-twinning behavior in BCC twin region, where both barriers are calculated by the twin growth fault energy profiles defined by a twinning pathway through homogeneous displacements near the pre-existing twin boundary (details in Figure 10). When we further increase VEC (around 4.34 at 300 K), ω phases at twin boundaries behave beneficially and they reduce the critical resolved shear stress (only $\sim$ 0.1 GPa along twin Burgers vector on twin planes) for twin boundary migration and {112} twin embryos can smoothly grow. When VEC further increases (greater than 4.5 at 300K), β to ω phase transformations are not favorable at twin boundaries, and {112} twin embryos can grow by standard twin dislocation formation/migration mechanism with relatively large critical stress ($\sim$ 0.3 GPa for VEC equal to 4.5 and $\sim$ 0.7 GPa for VEC equal to 5.0 (pure Nb)).

3) The effects of β to ω phase transformations on {112} twin embryo growth also depend on temperature. An increase in temperature can enhance the relative stability of β phase compared to other metastable phases, which can suppress the transformations detrimental to twin embryo growth, such as β to ω phase transformations at twin boundaries and reversible β to α'/α" phase transformations within the twin embryo. For example, a 9-layer twin embryo in Ti alloys with VEC equal to 4.25 can grow smoothly under small critical stress (only 0.2 $\sim$ 0.33 GPa) at 400 K.

4)The composition-and-temperature-dependent effects of ω phase on {112} twin embryo growth kinetics may originate from the free energy landscape of the homogeneous diffusionless β matrix $\rightarrow$ ω phase $\rightarrow$ β twin transformations illustrated in Figure 12.

Acknowledgement

GC and LQ gratefully thank the funding support from National Science Foundation, grant #CMMI-2121866. DL and YZ gratefully thank the funding support from National Science Foundation, grant #CMMI-2122272. The calculations were performed by using the Extreme Science and Engineering Discovery Environment (XSEDE) Stampede2 at the TACC through allocation TG-MR190035. This research was supported in part through computational resources and services provided by Advanced Research Computing Technology Services (ARC-TS), a division of Information and Technology Services (ITS) at the University of Michigan, Ann Arbor.

Conflict of interest

The authors declare that they have no conflict of interest.

Data availability

Data will be made available on reasonable request.

References

[1] P. Singh, H. Pungotra, and N. S. Kalsi, "On the characteristics of titanium alloys for the aircraft applications," Materials today: proceedings, vol. 4, no. 8, pp. 8971–8982, 2017.

[2] R. Boyer and R. Briggs, "The use of β titanium alloys in the aerospace industry," Journal of Materials Engineering and Performance, vol. 14, pp. 681–685, 2005.

[3] D. Banerjee and J. Williams, "Perspectives on titanium science and technology," Acta Materialia, vol. 61, no. 3, pp. 844–879, 2013.

[4] M. Marteleur, F. Sun, T. Gloriant, P. Vermaut, P. J. Jacques, and F. Prima, "On the design of new β-metastable titanium alloys with improved work hardening rate thanks to simultaneous trip and twip effects," Scripta Materialia, vol. 66, no. 10, pp. 749–752, 2012.

[5] C. Brozek, F. Sun, P. Vermaut, Y. Millet, A. Lenain, D. Embury, P. Jacques, and F. Prima, "A β-titanium alloy with extra high strain-hardening rate: Design and mechanical properties," Scripta Materialia, vol. 114, pp. 60–64, 2016.

[6] C. Leyens and M. Peters, Titanium and titanium alloys: fundamentals and applications. Wiley Online Library, 2006.

[7] M. Niinomi and C. J. Boehlert, "Titanium alloys for biomedical applications," Advances in metallic biomaterials: tissues, materials and biological reactions, pp. 179–213, 2015.

[8] A. Dan, E. M. Cojocaru, D. Raducanu, A. Nocivin, I. Cinca, and V. D. Cojocaru, "{332}⟨113⟩ and {112}⟨111⟩ twin variant activation during cold-rolling of a ti-nb-zr-ta-sn-fe alloy," Materials, vol. 15, no. 19, p. 6932, 2022.

[9] J. Zhang, F. Sun, Z. Chen, Y. Yang, B. Shen, J. Li, and F. Prima, "Strong and ductile beta ti–18zr–13mo alloy with multimodal twinning," Materials research letters, vol. 7, no. 6, pp. 251–257, 2019.

[10] H. Kim, Y. Ikehara, J. I. Kim, H. Hosoda, and S. Miyazaki, "Martensitic transformation, shape memory effect and superelasticity of ti–nb binary alloys," Acta materialia, vol. 54, no. 9, pp. 2419–2429, 2006.

[11] H. Y. Kim and S. Miyazaki, "Martensitic transformation and superelastic properties of ti-nb base alloys," Materials Transactions, vol. 56, no. 5, pp. 625–634, 2015.

[12] T. Saito, T. Furuta, J.-H. Hwang, S. Kuramoto, K. Nishino, N. Suzuki, R. Chen, A. Yamada, K. Ito, Y. Seno et al., "Multifunctional alloys obtained via a dislocation-free plastic deformation mechanism," Science, vol. 300, no. 5618, pp. 464–467, 2003.

[13] Y. Zhu, X. Liao, and X. Wu, "Deformation twinning in nanocrystalline materials," Progress in Materials Science, vol. 57, no. 1, pp. 1–62, 2012.

[14] M. Lai, C. C. Tasan, J. Zhang, B. Grabowski, L. Huang, and D. Raabe, "Origin of shear induced β to ω transition in ti–nb-based alloys," Acta Materialia, vol. 92, pp. 55–63, 2015.

[15] A. Crocker, "Twinned martensite," Acta Metallurgica, vol. 10, no. 2, pp. 113–122, 1962.

[16] Q. Liang, Z. Kloenne, Y. Zheng, D. Wang, S. Antonov, Y. Gao, Y. Hao, R. Yang, Y. Wang, and H. L. Fraser, "The role of nano-scaled structural non-uniformities on deformation twinning and stress-induced transformation in a cold rolled multifunctional β-titanium alloy," Scripta Materialia, vol. 177, pp. 181–185, 2020.

[17] F. Sun, J. Zhang, M. Marteleur, T. Gloriant, P. Vermaut, D. Laillé, P. Castany, C. Curfs, P. Jacques, and F. Prima, "Investigation of early stage deformation mechanisms in a metastable β titanium alloy showing combined twinning-induced plasticity and transformation-induced plasticity effects," Acta Materialia, vol. 61, no. 17, pp. 6406–6417, 2013.

[18] M. Hida, E. Sukedai, C. Henmi, K. Sakaue, and H. Terauchi, "Stress induced products and ductility due to lattice instability of β phase single crystal of ti-mo alloys," Acta Metallurgica, vol. 30, no. 8, pp. 1471–1479, 1982.

[19] S. Hanada and O. Izumi, "Correlation of tensile properties, deformation modes, and phase stability in commercial β-phase titanium alloys," Metallurgical and Materials Transactions A, vol. 18, pp. 265–271, 1987.

[20] M. J. Blackburn and J. A. Feeney, "Stress-induced transformations in ti-mo alloys," BOEING CO RENTON WA COMMERCIAL AIRPLANE GROUP, Tech. Rep., 1970.

[21] S. Hanada and O. Izumi, "Transmission electron microscopic observations of mechanical twinning in metastable beta titanium alloys," Metallurgical Transactions A, vol. 17, pp. 1409–1420, 1986.

[22] I. Gutierrez-Urrutia, C. L. Li, X. Ji, S. Emura, and K. Tsuchiya, "Twinning and detwinning mechanisms in beta-ti alloys," in Materials Science Forum, vol. 941. Trans Tech Publ, 2019, pp. 821–826.

[23] H. Tobe, H. Y. Kim, T. Inamura, H. Hosoda, and S. Miyazaki, "Origin of {3 3 2} twinning in metastable β-ti alloys," Acta materialia, vol. 64, pp. 345–355, 2014.

[24] X. Min, K. Tsuzaki, S. Emura, and K. Tsuchiya, "Enhancement of uniform elongation in high strength ti–mo based alloys by combination of deformation modes," Materials Science and Engineering: A, vol. 528, no. 13-14, pp. 4569–4578, 2011.

[25] S. Ozan, J. Lin, Y. Li, Y. Zhang, K. Munir, H. Jiang, and C. Wen, "Deformation mechanism and mechanical properties of a thermomechanically processed β ti–28nb–35.4 zr alloy," Journal of the mechanical behavior of biomedical materials, vol. 78, pp. 224–234, 2018.

[26] X. Min, K. Tsuzaki, S. Emura, and K. Tsuchiya, "Heterogeneous twin formation and its effect on tensile properties in ti–mo based β titanium alloys," Materials Science and Engineering: A, vol. 554, pp. 53–60, 2012.

[27] X. Min, X. Chen, S. Emura, and K. Tsuchiya, "Mechanism of twinning-induced plasticity in β-type ti–15mo alloy," Scripta Materialia, vol. 69, no. 5, pp. 393–396, 2013.

[28] S. A. Mantri, F. Sun, D. Choudhuri, T. Alam, B. Gwalani, F. Prima, and R. Banerjee, "Deformation induced hierarchical twinning coupled with omega transformation in a metastable β-ti alloy," Scientific reports, vol. 9, no. 1, p. 1334, 2019.

[29] E. Bertrand, P. Castany, I. Péron, and T. Gloriant, "Twinning system selection in a metastable β-titanium alloy by schmid factor analysis," Scripta materialia, vol. 64, no. 12, pp. 1110–1113, 2011.

[30] M. Lai, C. C. Tasan, and D. Raabe, "On the mechanism of {332} twinning in metastable β titanium alloys," Acta Materialia, vol. 111, pp. 173–186, 2016.

[31] J. Gao, Y. Huang, D. Guan, A. J. Knowles, L. Ma, D. Dye, and W. M. Rainforth, "Deformation mechanisms in a metastable beta titanium twinning induced plasticity alloy with high yield strength and high strain hardening rate," Acta Materialia, vol. 152, pp. 301–314, 2018.

[32] A. Cottrell and B. Bilby, "Lx. a mechanism for the growth of deformation twins in crystals," The London, Edinburgh, and Dublin Philosophical Magazine and Journal of Science, vol. 42, no. 329, pp. 573–581, 1951.

[33] J. W. Christian and S. Mahajan, "Deformation twinning," Progress in materials science, vol. 39, no. 1-2, pp. 1–157, 1995.

[34] S. L. Frederiksen and K. W. Jacobsen, "Density functional theory studies of screw dislocation core structures in bcc metals," Philosophical magazine, vol. 83, no. 3, pp. 365–375, 2003.

[35] J. Wang, Z. Zeng, C. R. Weinberger, Z. Zhang, T. Zhu, and S. X. Mao, "In situ atomic-scale observation of twinning-dominated deformation in nanoscale body-centred cubic tungsten," Nature materials, vol. 14, no. 6, pp. 594–600, 2015.

[36] A. Sleeswyk, "1/2¡ 111¿ screw dislocations and the nucleation of {112}¡ 111¿ twins in the bcc lattice," Philosophical Magazine, vol. 8, no. 93, pp. 1467–1486, 1963.

[37] S. Mahajan, "Accommodation at deformation twins in bcc crystals," Metallurgical Transactions A, vol. 12, pp. 379–386, 1981.

[38] A. Paxton, "Theoretical strength, twinning, antitwinning and pseudotwinning-a quantum-mechanical approach," in Symposium on Twinning in Advanced Materials, as part of the 1993 Materials Week. MINERALS, METALS & MATERIALS SOC, 1994, pp. 27–41.

[39] P. Bristowe, A. Crocker, and M. Norgett, "The structure of twin boundaries in body centred cubic metals," Journal of Physics F: Metal Physics, vol. 4, no. 11, p. 1859, 1974.

[40] V. Vitek, "Multilayer stacking faults and twins on {211} planes in bcc metals," Scripta Metallurgica, vol. 4, no. 9, pp. 725–732, 1970.

[41] V. Vítek, "Intrinsic stacking faults in body-centred cubic crystals," Philosophical Magazine, vol. 18, no. 154, pp. 773–786, 1968.

[42] S. Ogata, J. Li, and S. Yip, "Energy landscape of deformation twinning in bcc and fcc metals," Physical Review B, vol. 71, no. 22, p. 224102, 2005.

[43] A. Ojha and H. Sehitoglu, "Twinning stress prediction in bcc metals and alloys," Philosophical magazine letters, vol. 94, no. 10, pp. 647–657, 2014.

[44] M. Marteleur, H. Idrissi, B. Amin-Ahmadi, F. Prima, D. Schryvers, and P. Jacques, "On the nucleation mechanism of {112}¡ 111¿ mechanical twins in as-quenched β metastable ti-12 wt.% mo alloy," Materialia, vol. 7, p. 100418, 2019.

[45] B. Chen and W. Sun, "Omega transitional structure associated with {112}¡ 111¿ deformation twinning in a metastable beta ti-nb alloy, revealed by atomic resolution high-angle annular dark-field scanning transmission electron microscopy," Journal of Alloys and Compounds, vol. 766, pp. 123–130, 2018.

[46] S. Wu, D. Ping, Y. Yamabe-Mitarai, W. Xiao, Y. Yang, Q. Hu, G. Li, and R. Yang, "{1 1 2}¡ 1 1 1¿ twinning during ω to body-centered cubic transition," Acta materialia, vol. 62, pp. 122–128, 2014.

[47] M. Lai, C. C. Tasan, and D. Raabe, "Deformation mechanism of ω-enriched ti–nb-based gum metal: Dislocation channeling and deformation induced ω–β transformation," Acta Materialia, vol. 100, pp. 290–300, 2015.

[48] Y. Yang, P. Castany, E. Bertrand, M. Cornen, J. Lin, and T. Gloriant, "Stress release-induced interfacial twin boundary ω phase formation in a β type ti-based single crystal displaying stress-induced α" martensitic transformation," Acta Materialia, vol. 149, pp. 97–107, 2018.

[49] M. Li and X. Min, "Origin of ω-phase formation in metastable β-type ti-mo alloys: cluster structure and stacking fault," Scientific Reports, vol. 10, no. 1, pp. 1–15, 2020.

[50] X. Li, Q. Zhao, Y. Tian, Q. Wang, J. Fan, K. Song, H. Zhou, and J. Wang, "Phase transformation induced transitional twin boundary in body-centered cubic metals," Acta Materialia, p. 118815, 2023.

[51] H. Xing and J. Sun, "Mechanical twinning and omega transition by¡ 111¿{112} shear in a metastable β titanium alloy," Applied Physics Letters, vol. 93, no. 3, p. 031908, 2008.

[52] D. Ping, "Review on ω phase in body-centered cubic metals and alloys," Acta Metallurgica Sinica (English Letters), vol. 27, pp. 1–11, 2014.

[53] C. Cui and D. Ping, "Microstructural evolution and ductility improvement of a ti–30nb alloy with pd addition," Journal of alloys and compounds, vol. 471, no. 1-2, pp. 248–252, 2009.

[54] Y. Zhu, S. Zhu, and J.-F. Nie, "Atomic-scale study of {1 1 2} twin boundary structure in a β-ti alloy," Philosophical Magazine Letters, vol. 96, no. 7, pp. 280–285, 2016.

[55] A. Zunger, S.-H. Wei, L. Ferreira, and J. E. Bernard, "Special quasirandom structures," Physical review letters, vol. 65, no. 3, p. 353, 1990.

[56] A. Van de Walle, P. Tiwary, M. De Jong, D. Olmsted, M. Asta, A. Dick, D. Shin, Y. Wang, L.-Q. Chen, and Z.-K. Liu, "Efficient stochastic generation of special quasirandom structures," Calphad, vol. 42, pp. 13–18, 2013.

[57] G. Kresse and D. Joubert, "From ultrasoft pseudopotentials to the projector augmented-wave method," Physical review b, vol. 59, no. 3, p. 1758, 1999.

[58] G. Kresse and J. Furthmüller, "Efficiency of ab-initio total energy calculations for metals and semiconductors using a plane-wave basis set," Computational materials science, vol. 6, no. 1, pp. 15–50, 1996.

[59] M. Methfessel and A. Paxton, "High-precision sampling for brillouin-zone integration in metals," Physical Review B, vol. 40, no. 6, p. 3616, 1989.

[60] J. P. Perdew, K. Burke, and M. Ernzerhof, "Generalized gradient approximation made simple," Physical review letters, vol. 77, no. 18, p. 3865, 1996.

[61] G. Kresse and J. Hafner, "Ab initio molecular dynamics for liquid metals," Physical review B, vol. 47, no. 1, p. 558, 1993.

[62] P. E. Blöchl, "Projector augmented-wave method," Physical review B, vol. 50, no. 24, p. 17953, 1994.

[63] M. L. Waskom, "seaborn: statistical data visualization," Journal of Open Source Software, vol. 6, no. 60, p. 3021, 2021. [Online]. Available: https://doi.org/10.21105/joss.03021

[64] Y. Ikeda, K. Gubaev, J. Neugebauer, B. Grabowski, and F. Körmann, "Chemically induced local lattice distortions versus structural phase transformations in compositionally complex alloys," npj Computational Materials, vol. 7, no. 1, p. 34, 2021.

[65] S. Plimpton, "Fast parallel algorithms for short-range molecular dynamics," Journal of computational physics, vol. 117, no. 1, pp. 1–19, 1995.

[66] R. C. Ehemann and J. W. Wilkins, "Force-matched empirical potential for martensitic transitions and plastic deformation in ti-nb alloys," Physical Review B, vol. 96, no. 18, p. 184105, 2017.

[67] P. M. Larsen, S. Schmidt, and J. Schiøtz, "Robust structural identification via polyhedral template matching," Modelling and Simulation in Materials Science and Engineering, vol. 24, no. 5, p. 055007, 2016.

[68] T. Bonald, B. Charpentier, A. Galland, and A. Hollocou, "Hierarchical graph clustering using node pair sampling," arXiv preprint arXiv:1806.01664, 2018.

[69] A. Stukowski, "Visualization and analysis of atomistic simulation data with ovito–the open visualization tool," Modelling and simulation in materials science and engineering, vol. 18, no. 1, p. 015012, 2009.

[70] J. D. Honeycutt and H. C. Andersen, "Molecular dynamics study of melting and freezing of small lennard-jones clusters," Journal of Physical Chemistry, vol. 91, no. 19, pp. 4950–4963, 1987.

[71] D. Faken and H. Jónsson, "Systematic analysis of local atomic structure combined with 3d computer graphics," Computational Materials Science, vol. 2, no. 2, pp. 279–286, 1994.

[72] R. Gröger, J. Holzer, and T. Kruml, "Twinning and antitwinning in body-centered cubic metals," Computational Materials Science, vol. 216, p. 111874, 2023.

[73] E. Bitzek, P. Koskinen, F. Gähler, M. Moseler, and P. Gumbsch, "Structural relaxation made simple," Physical review letters, vol. 97, no. 17, p. 170201, 2006.

[74] Y. Hao, S. Li, S. Sun, C. Zheng, Q. Hu, and R. Yang, "Super-elastic titanium alloy with unstable plastic deformation," Applied Physics Letters, vol. 87, no. 9, 2005.

[75] Y. Hao, S. Li, S. Sun, and R. Yang, "Effect of zr and sn on young's modulus and superelasticity of ti–nb-based alloys," Materials Science and Engineering: A, vol. 441, no. 1-2, pp. 112–118, 2006.

[76] Y. Hao, S. Li, S. Sun, C. Zheng, and R. Yang, "Elastic deformation behaviour of ti–24nb–4zr–7.9 sn for biomedical applications," Acta biomaterialia, vol. 3, no. 2, pp. 277–286, 2007.

[77] Y. Wang, L.-Q. Chen, Z.-K. Liu, and S. Mathaudhu, "First-principles calculations of twin-boundary and stacking-fault energies in magnesium," Scripta Materialia, vol. 62, no. 9, pp. 646–649, 2010.

[78] B. Fan, X. Mei, K. Sun, and J. Ouyang, "Conducting polymer/carbon nanotube composite as counter electrode of dye-sensitized solar cells," Applied Physics Letters, vol. 93, no. 14, 2008.

[79] M. Lai, T. Li, and D. Raabe, "ω phase acts as a switch between dislocation channeling and joint twinning-and transformation-induced plasticity in a metastable β titanium alloy," Acta Materialia, vol. 151, pp. 67–77, 2018.

[80] S. Wang, M. Wu, D. Shu, G. Zhu, D. Wang, and B. Sun, "Mechanical instability and tensile properties of tizrhfnbta high entropy alloy at cryogenic temperatures," Acta Materialia, vol. 201, pp. 517–527, 2020.

[81] P. Bristowe and A. Crocker, "A computer simulation study of the structures of twin boundaries in body-centred cubic crystals," The Philosophical Magazine: A Journal of Theoretical Experimental and Applied Physics, vol. 31, no. 3, pp. 503–517, 1975.

[82] Z. Shi and C. V. Singh, "Competing twinning mechanisms in body-centered cubic metallic nanowires," Scripta Materialia, vol. 113, pp. 214–217, 2016.

[83] Y.-X. Feng, J.-X. Shang, Z.-H. Liu, and G.-H. Lu, "The energy and structure of (1 1 0) twist grain boundary in tungsten," Applied Surface Science, vol. 357, pp. 262–267, 2015.

[84] X. Min, P. Bai, S. Emura, C. Cheng, B. Jiang, K. Tsuchiya et al., "Effect of oxygen content on deformation mode and corrosion behavior in β-type ti-mo alloy," Materials Science and Engineering: A, vol. 684, pp. 534–541, 2017.

[85] K. Chou, N. Li, and E. A. Marquis, "Enhanced work hardening from oxygen-stabilized ω precipitates in an aged metastable β ti-nb alloy," Acta Materialia, vol. 220, p. 117302, 2021.

[86] K. Chou and E. A. Marquis, "Role of oxygen on the precipitation and deformation behavior of an aged β ti-15mo alloy," Journal of Alloys and Compounds, vol. 891, p. 161811, 2022.

[87] C. C. Bortolan, L. C. Campanelli, C. Paternoster, N. Giguere, N. Brodusch, C. Bolfarini, R. Gauvin, P. Mengucci, G. Barucca, and D. Mantovani, "Effect of oxygen content on the mechanical properties and plastic deformation mechanisms in the twip/trip ti–12mo alloy," Materials Science and Engineering: A, vol. 817, p. 141346, 2021.

[88] T. Furuta, S. Kuramoto, C. Rong, J. Hwang, K. Nishino, T. Saito, and M. Ikeda, "Effect of oxygen on phase stability and elastic deformation behavior in gum metal." Journal of the Japan Institute of Metals, vol. 70, no. 7, pp. 579–585, 2006.

[89] H.-p. Duan, H.-x. Xu, W.-h. Su, Y.-b. Ke, Z.-q. Liu, and H.-h. Song, "Effect of oxygen on the microstructure and mechanical properties of ti-23nb-0.7 ta-2zr alloy," International Journal of Minerals, Metallurgy, and Materials, vol. 19, pp. 1128–1133, 2012.

[90] X. Wang, L. Li, H. Xing, P. Ou, and J. Sun, "Role of oxygen in stress-induced ω phase transformation and {3 3 2}¡ 1 1 3¿ mechanical twinning in βti–20v alloy," Scripta Materialia, vol. 96, pp. 37–40, 2015.

[91] J. Williams, B. Hickman, and D. Leslie, "The effect of ternary additions on the decompositon of metastable beta-phase titanium alloys," Metallurgical Transactions, vol. 2, pp. 477–484, 1971.

[92] J. Ballor, T. Li, F. Prima, C. J. Boehlert, and A. Devaraj, "A review of the metastable omega phase in beta titanium alloys: The phase transformation mechanisms and its effect on mechanical properties," International Materials Reviews, vol. 68, no. 1, pp. 26–45, 2023.

[93] X. Min, S. Emura, K. Tsuchiya, T. Nishimura, and K. Tsuzaki, "Transition of multi-deformation modes in ti–10mo alloy with oxygen addition," Materials Science and Engineering: A, vol. 590, pp. 88–96, 2014.

[94] E. Faran and D. Shilo, "Twin motion faster than the speed of sound," Physical review letters, vol. 104, no. 15, p. 155501, 2010.